Increasing precipitation due to climate change could partially offset the impact of warming on glacier loss in the monsoon-influenced Himalaya until 2100 CE

Anya M. Schlich-Davies[1*], Ann V. Rowan[2*], Andrew N. Ross[1], Duncan J. Quincey[3], Vivi K. Pedersen[4]

[1]Priestley International Centre for Climate, School of Earth and Environment, University of Leeds, UK
[2]Department of Earth Science, University of Bergen and Bjerknes Centre for Climate Research, Bergen, Norway
[3]School of Geography, University of Leeds, UK
[4]Department of Geoscience, Aarhus University, Aarhus C, Denmark

*These authors contributed equally to this work
Correspondence to: Ann V. Rowan (ann.rowan@uib.no)

Abstract. Glacier volume in the Himalaya is projected to shrink by 53–70% by 2100 CE due to climate change. However, the impact of changes in precipitation amount and distribution on future glacier change remains uncertain because mesoscale meteorology is not represented in current models of glacier change. We explore the combined effects of past and future changes in air temperature and precipitation amount and distribution on the evolution of Khumbu Glacier in the Everest region of Nepal—a benchmark glacier in the monsoon-influenced Himalaya—using a climate-glacier modelling approach that forces an ice-dynamical glacier evolution model with surface mass balance forcings that includes mesoscale meteorological variables derived from downscaling of Regional Climate Model results. Our simulations show that historical warming has committed Khumbu Glacier to future volume loss of 10–23% during this century and that under an intermediate future emissions scenario (RCP4.5), Khumbu Glacier could lose 70% volume by 2100 CE due to warming. However, the projected increase in precipitation in tandem with warming could offset about half of the projected glacier loss, such that the total decrease in glacier volume by 2100 CE compared to the present day is only 34%. Under a high future emissions scenario (RCP8.5) glacier loss due to warming will not be compensated by changes in precipitation but will instead result in substantial ablation above 6,000 m that causes Khumbu Glacier to vanish by 2160–2260 CE.

1. Introduction

Projecting glacier change in response to climate change is important for determining the impact of anthropogenic warming on regional water availability (Pritchard, 2019). High Mountain Asia is projected to lose 34 ± 19% of glacier volume by 2100 CE if warming is limited to 1.5°C to meet the ambitious Paris Agreement target (Kraaijenbrink et al., 2017). More realistic projections of glacier change give 53 ± 23% volume loss by 2100 CE under the intermediate emissions scenario RCP4.5, and 69 ± 20% under the high emissions scenario RCP8.5 (Kraaijenbrink et al., 2017; Marzeion et al., 2020; Rounce et al., 2023). Such projections are challenging because accumulation and ablation processes in mountain environments are driven by orographic feedbacks between high-relief topography and atmospheric circulation systems such as the South Asian Summer Monsoon (Bookhagen and Burbank, 2006). Furthermore, large uncertainties arise from the challenge of simulating the interactions between the mass balance regimes of monsoon-influenced glaciers, where accumulation and ablation both occur during the monsoon season, and the dynamics of glaciers flowing through high-relief topography, such as the development of supraglacial debris layers that modify surface melting (Dehecq et al., 2019; Miles et al., 2018b; Salerno et al., 2023). Variability in the extent and intensity of the Indian Summer Monsoon during the Last Glacial Maximum affected glacier expansion the monsoon-influenced Himalaya through changes in snowfall distribution (Benn and Owen, 1998; Owen et al., 2009). Future Indian Summer Monsoon precipitation and variability is projected by Global Circulation Models (GCMs) to increase with current global warming (Katzenberger et al., 2021), but the effect on Himalayan glacier volume of projected changes in precipitation amount, timing, and phase (snow/rain) remain poorly constrained (Immerzeel et al., 2012; Mölg et al., 2014; Ragettli et al., 2016; Shaw et al., 2022; Shea et al., 2015).

Supraglacial debris covers 4–7% of glacier surfaces globally and 30% of glacier ablation areas in the Himalaya and acts to modify glacier response to climate change from regional trends (Herreid and Pellicciotti, 2020; Kraaijenbrink et al., 2017; Rounce et al., 2023; Rowan et al., 2015). Satellite observations show that the rate of glacier loss across the Himalaya has accelerated over the last 40 years for both clean-ice glaciers and debris-covered glaciers (Maurer et al., 2019). Observations and glacier models indicate that thick supraglacial debris has caused historical mass loss from debris-covered glaciers to lag that of clean-ice glaciers, such that debris-covered glaciers are currently larger than would otherwise be the case (King et al., 2020; Rounce et al., 2023; Rowan et al., 2021). However, the dampening effect of supraglacial debris on net glacier melt is now being overturned by the development of extensive supraglacial ponds and ice cliffs within debris layers (Miles et al., 2018a; Strickland et al., 2023) and the stagnation and detachment of debris-covered tongues from the upper and more active sections of glaciers (Rowan et al., 2021). Models of debris-covered glacier evolution represent the dynamic feedback between debris transport, mass balance and ice flow that differentiates the evolution of glaciers with a substantial supraglacial debris layer from climatically-equivalent clean-ice glaciers (Zekollari et al., 2022). Such models require numerical representation of the processes controlling debris delivery to glacier surfaces from hillslope erosion, englacial transport of debris through the glacier to accumulate at the ice surface in the ablation area, and the impact of an evolving supraglacial debris layer on surface melting (Nicholson et al., 2021). These processes can be considered in 2-D (along the glacier flowline) either considering stochastic debris delivery to the glacier (Vacco et al., 2010; Wirbel et al., 2018) or continuous debris delivery, which can result in the over-accumulation of debris at the terminus (Anderson and Anderson, 2016; Ferguson and Vieli, 2020; Jouvet et al., 2011), or in 3-D (using the horizontal and vertical ice flow fields), which allows the lateral transport and deposition of debris to the margins of the ablation area (Rowan et al., 2015).

The high proportion of debris-covered glaciers in the monsoon-influenced Himalaya could significantly affect regional glacier change, and yet few studies currently consider the impact of supraglacial debris on glacier mass balance because impact of supraglacial debris on glacier change remains challenging to simulate at a regional or global scale (Compagno et al., 2022; Nicholson et al., 2021; Rounce et al., 2023). Glacier models at these scales treat supraglacial debris as static and do not yet account for the dynamic evolution of debris thickness and distribution in response to changes in mass balance and ice flow. Quantifying the impact of feedbacks set up by the formation and expansion of supraglacial debris layers at a regional scale requires exploring these processes at scales that can be resolved in ice-dynamical glacier evolution models (Rowan et al., 2015). While recent rapid warming resulted in a rise in regional equilibrium line altitude causing recession and collapse of glacier termini for both clean-ice glaciers and debris-covered glaciers, the decay of the former ablation areas of debris-covered glaciers is delayed by the insulation of the ice surface by supraglacial debris, such that the terminus of the actively flowing glacier can remain in contact with the detached ice tongue rather than separating (Maurer et al., 2019; Pellicciotti et al., 2015; Rowan et al., 2021). In common with most large debris-covered Himalayan glaciers, Khumbu Glacier in the Everest region of Nepal is in greater imbalance with climate than a climatically equivalent clean-ice glacier, and has maintained a more extensive ice volume than would be possible without supraglacial debris (Rowan et al., 2021). However, as a result of reduced ice flux from the accumulation area, the debris-covered tongue no longer receives much or any input of ice, and has dynamically detached from the active glacier (Fig. 1c); this observation is confirmed by the rapid reduction in ice flow and the peak in glacier surface lowering below the Khumbu Icefall where the debris layer is thinnest (King et al., 2020; Quincey et al., 2009). Therefore, the active glacier and the stagnant debris-covered tongue will evolve along different trajectories and only the part of Khumbu Glacier above the terminus of the active glacier (Fig. 1) can be considered dynamic. Projections of future glacier evolution should discount the heavily debris-covered former tongue that is decaying *in situ* without any input of new ice from the accumulation area while considering the development of supraglacial debris across the ablation area of the active glacier.

We use a novel climate-glacier model of Khumbu Glacier to test the hypothesis that changes in precipitation in response to climate change will reduce the impact of warming on glacier mass loss. Khumbu Glacier is a benchmark debris-covered glacier in the monsoon-influenced Himalaya flowing from 7,981 m above sea level (a.s.l.) to 4,879 m a.s.l. that is representative of the majority of glaciers in this region (Fig. 1). We use a climate-glacier model forced by mesoscale meteorological variables to simulate the evolution of Khumbu Glacier from the late Holocene (~1 ka) through the present day (2015 CE) until 2100 CE using results from three downscaled Regional Climate Models (RCMs) under two Relative Concentration Pathways (RCPs). This approach represents an advance in the use of such models to understand the evolution of Himalayan glaciers, as for the first time mesoscale meteorological forcing is used with a model that represents the processes of sublimination and snow avalanching, which are important controls on the mass balance of high-elevation glaciers. The simulations start from the late Holocene because this is the period when Khumbu Glacier was last in dynamic equilibrium with the local climate as evidenced by the large ice-marginal moraines dated to 1.3 ± 0.1 ka surrounding the present-day glacier (Hornsey et al., 2022) when the glacier surface was free of debris (Rowan et al., 2015) and continue to 2300 CE using the best available projections of longer-term climate change. The focus of our experiments is to simulate glacier evolution to the end of the 21st Century, but the centennial dynamic response time of a large debris-covered glacier such as Khumbu Glacier means that the glacier continues to evolve beyond this time scale, and we continued our simulations through the subsequent two centuries to explore longer-term glacier evolution.

2. Climate-glacier modelling of Khumbu Glacier

The climate-glacier model experiments use mesoscale meteorological variables at an appropriate scale to calculate surface mass balance at high elevations in the monsoon-influenced Himalaya in combination with a debris-covered glacier evolution model to represent the surface processes that modify mass balance (Fig. 2). Our approach produces a total of six simulations of Khumbu Glacier from three RCMs and two RCPs (RCP4.5 and RCP8.5; Collins et al., 2013) to explore the impacts of possible variability in future precipitation amount and distribution in tandem with warming on glacier evolution. The experimental design represents an advance compared with previous climate-glacier modelling efforts through including robust representations of (1) mesoscale meteorological phenomena including sublimation, (2) the redistribution of surface mass balance by snow avalanching, and (3) the feedbacks between debris transport and mass balance. We use RCMs to force the future climate scenarios and first evaluate their capabilities against observations of present-day weather and climate. In each simulation, we use climate time slices representing the present day (2015–2020 CE) and the end of the 21st Century (2095–2100 CE) to calculate surface mass balance. The five-year time slices were chosen to reduce the computational expense of the climate-glacier modelling (~24 hours per simulation) and the preceding decade was used to evaluate these time slices. The three RCMs and two future RCPs represent a range of possible future climates including distinctly different precipitation trends (Table 1) and are used as inputs to the surface energy balance model COSIPY (Sauter et al. 2020). The resulting six mass balances (present day and future for each RCM) force the glacier model (Rowan et al., 2015) from the late Holocene (~1 ka) through the present day until 2100 CE, beyond which period only less detailed climate projections are available. Given the absence of regional climate projections beyond 2100 CE, globally projected temperature changes were used to extend the end-of-century mass balances for RCP4.5 and RCP8.5, giving a further increase in temperature of 0.5 °C by 2200 CE and 0.7 °C by 2300 CE under RCP4.5, and 2.8 °C by 2200 CE and 4.1 °C by 2300 CE under RCP8.5 (Table 1; Collins et al., 2013). No precipitation changes were applied to the post-2100 CE climates due to the absence of projections for precipitation in the CORDEX RCMs and high uncertainty in global precipitation changes for this period.

2.1 Present-day RCM downscaling using meteorological observations

Six RCMs were assessed on their fidelity to present-day climate, known as hindcasting (Biemans et al., 2013), with emphasis on temperature seasonality and seasonal precipitation dynamics given the importance of these variables for glacier mass balance. RCMs from the Coordinated Regional Downscaling Experiment (CORDEX) South Asia domain that were dynamically downscaled from CMIP5 GCMs by the Indian Institute of Tropical Meteorology to a 50 km spatial resolution (Lutz et al.,

2016) were downloaded for the grid box containing Khumbu Glacier (27.9065056°N, 86.4352951°E) that has an elevation of about 2,100 m a.s.l.. Three of the six CORDEX South Asia RCMs (NOAA, CCCma, IPSL) that were observed to span a range of possible future precipitation conditions (Table 1) were selected as discrete scenarios for the climate-glacier model experiments. The three remaining RCMs were discounted due to being intermediate to those selected for our experiments (i.e. close to the future precipitation scenario represented by CCCma) or particularly poor at reproducing seasonal temperature and precipitation cycles. For example, despite the annual precipitation sums from the CSIRO RCM being closest to observed values and having the potential to be the 'driest' scenario examined, analysis of precipitation seasonality indicated that the monsoon signal was completely absent with a strong dominance of winter precipitation in the results of this RCM.

The NOAA RCM is characterised by the highest annual precipitation amount, the IPSL RCM is characterised by the lowest annual precipitation, and the CCCma RCM is characterised by an intermediate value for precipitation, giving a range of dry to wet future precipitation distributions relative to the present day that span the range of possible future precipitation scenarios. The three RCMs were downscaled using observations from three high-elevation automatic weather stations (AWS; Fig. 1c) collected between January 2006 and November 2019 with gaps filled with interpolated data from neighbouring stations where possible (Fig. 2). The present-day RCM results were downscaled using quantile mapping, also known as "distribution mapping", using 14 years of observations from the three AWS. Parametric quantile mapping (Piani et al., 2010) was used, whereby a statistical relationship between the raw climate model outputs and observations is formed by substituting the RCM results with observations at a cumulative density function of the prescribed distribution (e.g., a gaussian distribution for temperature; Luo et al., 2018; a gamma distribution for precipitation; Piani et al., 2010). This correction was then applied to the raw RCM outputs to produce a third downscaled dataset that improved the fit to observations (Maraun et al., 2016). The quantile mapping approach is effective for downscaling precipitation and reduces errors in the standard deviation, the coefficient of variation, and the skewness of distributed values relative to other methods (Lafon et al., 2012; Reiter et al., 2018). The 14 years of AWS data were also used to disaggregate the resultant daily downscaled present-day and end-of-century climate model outputs to an hourly resolution for energy balance modelling. All meteorological variables, excluding precipitation, were downscaled using the MELODIST Python tool (Förster et al., 2016). Seasonal means were applied for precipitation to reproduce the 'nocturnal peak' seen during the monsoon that MELODIST was unable to replicate.

14 years of meteorological observations were collected from two AWS at the Pyramid Observatory at 5,050 m a.s.l and 5,035 m a.s.l. and the West Changri Nup Glacier AWS at 5,363 m a.s.l.. Missing data were replaced through interpolation with an alternative AWS from this group. Precipitation was measured at 15-minute intervals using a Geonor T-200BM sensor mounted 1.8 m above the surface. Evaporation from the bucket is supposedly blocked by a layer of oil but some does occur as evidenced by precipitation values below 0 mm. Noise from wind and evaporation were corrected for by compensating any negative change over the 15-minute time step with the neighbouring positive value such that accumulated precipitation was unchanged. Periods with prolonged evaporation were set to zero. Undercatch of snowfall by rainfall gauges was corrected through precipitation phase partitioning using wind speed observations (Wagnon et al., 2009). For interpolation of air temperature, hourly lapse rates were used that averaged 0.00554 °C m^{-1} to adjust to the height of the reference point at 5,050 m a.s.l.. Where possible, precipitation data taken from the Pyramid AWS at 5,035 m a.s.l. because this precipitation gauge provides a longer period of continuous observations than the other gauges and avoids errors due to low precipitation amounts measured by tipping bucket gauges, which are known to systematically underestimate snowfall, particularly during high winds (Sherpa et al., 2017). Further information on RCM downscaling and AWS data analysis are provided in Appendix A.

2.2 Future RCM downscaling

Two future emission scenarios (RCP4.5 and RCP8.5) are available from CORDEX South Asia, which represent only intermediate and high emissions by 2100 CE relative to the present day. These two emissions scenarios are frequently used in climate impact studies, enabling the comparison of our results with studies that use other climate model or glacier model projections. The two future emissions scenarios were analysed for each of the three CORDEX RCMs to account for the inherently high uncertainties in future precipitation trends associated with climate models and the interplay of changing precipitation with atmospheric warming. The same statistical downscaling approach and disaggregation used for the three present-day RCMs (described in Section 2.1) was applied to the raw CORDEX RCM daily outputs for the three future RCM time slices under RCP4.5 and RCP8.5. The temperature change between the present day and the future time slices was preserved and there was no evidence of any imposed strengthening in the monsoon resulting from this downscaling. An increase in the frequency of days per year outside of the monsoon season with high precipitation amounts (defined here as over 15 mm of daily precipitation) accounts in large part for the higher annual precipitation amounts relative to present day found in four out of the six RCMs. However, the total future annual precipitation increase is on average 8.8% greater in the downscaled climates relative to the raw RCMs, suggesting this positive trend was inflated following downscaling. The downscaled climates reduced the frequency of precipitation, although, as in present day observations, monsoon precipitation occurs frequently and can be characterised as predominantly drizzle into the future.

2.3 Surface energy and mass balance calculations

The Coupled Snowpack and Ice-surface Energy and Mass Balance model in Python (COSIPY) was used to calculate surface energy balance (Sauter et al., 2020). COSIPY is developed and modularised in Python and integrates a surface energy balance model with a multi-layer snow and ice model and thereby resolves all energy fluxes at the ice surface that contribute to surface melt. COSIPY was chosen as it is currently considered a leading open-source method for estimating glacier mass balance and has previously been applied to glaciers in High Mountain Asia. COSIPY includes a calculation of sublimation, which is an important ablation process for high-elevation glaciers (Bonekamp et al., 2021; Brun et al., 2023; Huintjes et al., 2015). The COSIPY model domain was taken from the 30-m digital elevation model (DEM) acquired from the Shuttle Radar Topography Mission (Farr et al., 2007) that was resampled to 100-m grid spacing following sensitivity analyses that revealed minimal impact on the results whilst greatly reducing computational expense. CORDEX RCM daily climate variables (temperature, precipitation, the radiation components, wind speed, relative humidity and atmospheric pressure) were used to force COSIPY. Snowfall measurements can be used as an input to COSIPY, but precipitation was partitioned into rainfall and snowfall using the snow transfer scheme within COSIPY given the paucity of observations and high uncertainties associated with AWS observations, climate reanalysis, and modelled snowfall products for this region (Sauter et al., 2020). COSIPY was forced using hourly meteorology with nine variables to calculate the energy balance and mass balance components at an hourly time step from the sum of accumulation by solid precipitation, deposition, and refreezing of melt water percolation, and ablation by melt and sublimation (Fig. 3). The impacts of supraglacial debris on ablation and the impacts of snow avalanching on accumulation were handled in the glacier evolution model. Further information on the use and evaluation of COSIPY is provided in Appendix B.

2.4 Glacier evolution modelling

The second-order shallow ice approximation model (iSOSIA) is a 3-D higher-order ice-dynamical glacier evolution model that solves for the flow of ice including longitudinal and transverse stress gradients that are imposed on ice flow through high-relief topography (Egholm et al., 2011). While previous versions of this glacier model used depth-integrated ice flow, the version used here, and earlier studies, to simulate the evolution of Khumbu Glacier is fully 3-D as the ice thickness is divided into 20 vertical layers to allow for the calculation of englacial debris transport (Rowan et al., 2015). The glacier model has a variable time step that can adjust up to a maximum of 0.1 years to allow greater computational efficiency. This glacier model simulates the evolution of debris-covered glaciers by incorporating the feedbacks between debris transport, mass balance and ice flow (Rowan et al., 2015) and includes two processes that are important for many Himalayan glaciers—the redistribution of snow by avalanching that is estimated to account for 75% of glacier accumulation, and the formation of a supraglacial debris layer that insulates the ice surface to modify ablation (Fig. 1d) (Rowan et al., 2015).

The distributed surface mass balances calculated using COSIPY and forced using the downscaled RCMs for the periods 2015–2020 CE and 2095–2100 CE were used as inputs to the glacier model with no change in forcing applied between time steps. Surface processes within the glacier model modified the distribution of accumulation and ablation but this was not updated into the surface topography used in COSIPY. Simulated accumulation was the result of the total snowfall in each cell and avalanching of snow imposed for the accumulated snowpack from hillslopes by removing snow and ice from hillslopes greater than 28° and redistributing this mass across less steep surfaces using a non-linear hillslope flux model (Roering et al., 1999). The avalanching routine was previously applied to Khumbu Glacier and found to be sufficient to prevent snow and ice accumulation on slopes that are observed to be free of glacier ice such as the southwest face of Sagarmatha (Mt. Everest) whilst allowing accumulation on steep sections of the glacier (Rowan et al., 2015). The critical slope of 28° was selected because this threshold is low enough to prevent ice accumulation on slopes that are clearly ice-free today, but high enough to produce accumulation rates at the glacier surface that are in line with the limited available observations for Himalayan glaciers of 2 m water equivalent (w.e.) per year (Benn and Lehmkuhl, 2000). Rock avalanching is responsible for much of the debris accumulation on the glacier surface, but there is little information about the magnitude and frequency of these events so headwall erosion was assumed to be uniform at 1 mm a^{-1} (Rowan et al., 2021). Debris produced by headwall erosion was delivered to the glacier surface using a similar non-linear hillslope flux model to snow avalanching. The reduction in ablation beneath supraglacial debris from clean-ice values was represented as a reciprocal function that scales clean-ice ablation (b_{clean}) to give sub-debris melt (b_{debris}) as a function of debris thickness (h):

$$b_{debris} = b_{clean} \times \frac{h_0}{h + h_0} \qquad \text{Eq. (1)}$$

where h_0 is a constant representing the characteristic debris thickness at which the reduction in ablation due to insulation by supraglacial debris is 50% of the value for an equivalent clean-ice surface (Anderson and Anderson, 2016; Rowan et al., 2021). The observed heterogeneity of ablation on the surface of Khumbu Glacier requires a parameterisation of sub-debris melt that represents the effects of differential ablation, which is represented in Equation (1) by the value of 0.8 m chosen for h_0 that represents a positively skewed supraglacial debris thickness distribution including ablation 'hotspots' such as supraglacial ponds and ice cliffs, and is representative of the current state of Khumbu Glacier (Bartlett et al., 2021; Rowan et al., 2021; Strickland et al., 2023).

2.5 Climate-glacier model experimental design

The late Holocene (~1 ka) glacier was reconstructed using a 5000-year equilibrium simulation starting from an ice-free domain and used as the starting point for three transient simulations through the 'Little Ice Age' maximum forced by a step change in mean annual air temperature (MAAT) equivalent to 1.5°C colder than the present day (Appendix B). The simulation was then forced to present-day conditions using the three surface mass balances (one for each RCM) calculated using COSIPY. The simulations continued to 2100 CE forced by the distributed surface mass balances calculated for each of the three RCMs and two RCPs using COSIPY. Khumbu Glacier is surrounded by ice-marginal moraines denoting the late Holocene (1.3 ± 0.1 ka) extent and ice thickness (Hornsey et al., 2022), which are used to constrain the spin-up simulation. Observations and modelling of the dynamics and structure of Khumbu Glacier show that the lower 5 km (25% of the total length, 20% of total ice volume) is stagnant and has dynamically detached from the active glacier in the last century (Miles et al., 2021; Quincey et al., 2009; Rowan et al., 2021). Basal ice at the glacier surface indicates that the active terminus overrides the stagnant glacier tongue (Miles et al., 2021) and measurements of surface displacement show no longitudinal flow through the detached debris-covered tongue, which is collapsing laterally at a rate of about 3 m a^{-1} (Watson et al., 2017). We therefore simulate only the active section of the glacier and assigned the detached debris-covered tongue to the model domain as a static topographic feature. The ice-free domain was found by subtracting estimated ice thickness (Farinotti et al., 2019) from the 30-m DEM. The ice-free model domain incorporated the full hydrological catchment including the steep hillslopes in the Western Cwm that provide snow to the glacier surface by avalanching. The late Holocene to present-day spin-up simulations of Khumbu Glacier were evaluated against a range of observations at the present day, and the simulation forced using the NOAA RCM was identified as the starting point for all future simulations because this was most representative of the observed present-day state of the glacier. For more detail on the glacier model parameterisation and evaluation of the present-day simulation using geological and remote sensing observations of the current state and recent change of Khumbu Glacier, we refer to (Rowan et al., 2021) a summary of which is presented in Appendix B.

3. Results

3.1 Evaluation of the present-day climate-glacier model results

Each of the downscaled climate variables from the three RCMs for the present-day time slices (2015–2020 CE) are evaluated against 14 years of observations from three AWS to assess the representation of means, seasonality, diurnal cycles, day-to-day variability, and interannual variability. All three downscaled RCMs show good agreement in their mean annual air temperatures (–2.15 ± 0.05°C) and with observed air temperatures from the Pyramid AWS (Appendix A). The representation of the monsoon is greatly improved by the RCM downscaling; temperature seasonality is well resolved following quantile mapping and the monthly mean and minimum air temperatures are similar to observations across the present-day time slices (Fig. A1). The monsoon stabilises air temperatures and reduces the range between minimum and maximum temperatures in the downscaled RCMs, which is in better agreement with AWS observations, but does not occur in the raw RCMs. We note that the downscaled maximum temperature is at times higher than observations amongst all RCMs during the post-monsoon and winter, but that the distribution of downscaled temperatures is similar to observed values (Fig. A2). Gamma distribution quantile mapping substantially improves the absolute precipitation values relative to the AWS observations compared to those in the raw RCMs; the overestimation of winter precipitation and relative underestimation of monsoon precipitation amounts in the raw RCMs is reduced and downscaled results show a clearer monsoon signal (Fig. A3). When compared with AWS observations, RCM downscaling slightly over-corrects the seasonal precipitation pattern with a slight underestimation of winter precipitation for the most extreme winter events. Across the three present-day simulations, the surface mass balance calculated using the NOAA RCM is more positive than for the ISPL and CCCma RCMs and most similar to the mass balance calculated from meteorological observations.

The simulated glacier geometry and dynamics (Fig. 4) are compared with remotely sensed observations of velocity, surface elevation change, and debris cover extent for the present-day glacier and moraine positions indicating the extent during the late Holocene (~1 ka) and Little Ice Age (~500 a) maxima (Hornsey et al., 2022) are compared to the equivalent periods in the simulation (Appendix B). The distributed surface mass balances calculated using COSIPY are most similar to observed values after the calculated surface mass balances are integrated with the glacier model to include accumulation by snow avalanching and the reduction in surface melting beneath supraglacial debris; the glacier extent is underestimated if supraglacial debris is not simulated (Fig. 5). The supraglacial debris-mass balance feedback in the glacier model reproduces the observed reversed mass balance gradient and peak in ablation below the Khumbu Icefall (Fig. 1) (Benn and Lehmkuhl, 2000; King et al., 2020). The simulated glacier area was 7.8 km^2—similar to that obtained from structural mapping in 1979 CE (Nakawo, 1986). Radio-echo sounding in 1999 CE obtained ice thickness estimates close to the active terminus of ~160 m (Gades et al., 2000) and simulated ice thickness at the terminus was 130 m. The simulated active terminus thickness is approximately 175 m in 1999 CE, which agrees well with observations from DEMs of difference that show thinning here of up to 55 m between 1984–2018 CE (King et al., 2020). Simulated surface elevation change in the ablation area is –30 m over 20 years to the present day and similar to values derived from satellite observations for 1984–2015 CE (King et al., 2020). Simulated present-day glacier velocities (Fig. 6) show a similar pattern and magnitude to glacier surface velocities observed using remote sensing observations that reach a maximum of 220 m a^{-1} in the Khumbu Icefall (Altena and Kääb, 2020) and up to 20 m a^{-1} in the ablation area (Quincey et al., 2009; Dehecq et al. 2019). The simulated present-day velocities in this study are a better fit to remote sensing observations than those from previous simulations that used an elevation-dependent mass balance forcing (Rowan et al., 2015, 2021) where the maximum simulated velocities were 118 m a^{-1}.

3.2 Climate change and glacier evolution from the present day until 2100 CE

Khumbu Glacier is responding to historical climate change and will continue to shrink even if warming ceases today. Indeed, if we allow the spin-up experiment to reach equilibrium with the present-day NOAA RCM mass balance, the glacier terminus will recede by 2.1 km and the maximum ice thickness will decrease from 246 m to 206 m by 2100 CE without any additional warming (Fig. 7a). In this simulation, a supraglacial debris layer up to 1.3 m thick extends 1 km up-glacier from the terminus and partially dampens the committed volume loss by sustaining 13% more ice volume than would be the possible for a clean-ice glacier surface with the same mass balance. The committed glacier volume loss due to historical warming in the absence of any further climate forcing is 10–23% of the present-day glacier volume (Fig. 7b) with the uncertainty represented by this range of values arising from the parameterisation of the impact of supraglacial debris evolution on surface melting.

Greater warming occurs in winter than in summer under both RCPs (Sanjay et al., 2017) and results in an increase in annual precipitation amount of about 15%, made up of a greater increase in winter precipitation than summer precipitation. The climate forcing from the downscaled NOAA RCM under RCP4.5 is 1.4°C warmer than the present day (–0.75°C in 2095–2100 CE compared with –2.15°C in 2015–2020 CE) and annual precipitation increases by 14.8% from 581.4 mm at present day to 664.8 mm a^{-1} by 2100 CE with summer (June–September) precipitation increasing by 5.4% and winter (December–February) precipitation increasing by 14.1% (Fig. 2). Under RCP8.5, the downscaled climate forcing is projected to be 3.8°C warmer than present day (1.65°C in 2095–2100 CE) with an increase in annual precipitation of 14.9% by 2100 CE, with summer precipitation increasing by 9.8% and winter precipitation increasing by 19.4%. The spatially averaged cumulative glacier mass balance is –0.14 m w.e. a^{-1} in 2100 CE, which is slightly more positive than the present-day value of –0.21 m w.e. a^{-1}. In the NOAA RCM RCP4.5 experiment, glacier volume decreased by 36% between the present day and 2100 CE (Fig. 7). While significant, the end-of-century glacier loss is partially offset by the concurrent increase in precipitation. In comparison, an equivalent simulation forced only by warming and without any change in precipitation results in a more linear trajectory of glacier change and 70% loss of glacier volume by 2100 CE (Fig. 8) demonstrating that 34% of potential glacier loss from warming could be compensated by the increase in precipitation that occurs as a result of warming.

The CCCma and IPSL RCMs project greater warming from the present day by 2100 CE than the NOAA RCM under RCP4.5 with a value of 1.6°C (+0.2°C compared with the NOAA RCM) in the IPSL RCM experiment and 2.2°C (+0.8°C) in the CCCma RCM experiment. These two RCMs also project slightly greater warming by 2100 CE under RCP8.5, with a value of 3.9°C (+0.1°C compared with the NOAA RCM) for the IPSL RCM experiment and 4.1°C (+0.3°C) for the CCCma RCM experiment. The projected increase in precipitation amount across the three RCMs is similar between RCPs with annual totals above 600 mm by 2100 CE. The CCCma RCM gives the greatest increase in annual precipitation amount of 100 mm by 2100 CE. There is no evidence of change in the intensity of the Indian Summer Monsoon, as the seasonal split in precipitation remains similar to the present day, but the frequency of days with high precipitation (over 15 mm per day) increases by 2100 CE, giving twice as many days in the NOAA RCM experiment and up to seven times as many days in the IPSL RCM experiment. Under RCP8.5, all experiments show similar results for mass balance by 2100 CE with only a 10% difference in glacier volume between the three RCMs (Fig. 7). The CCCma RCM experiment has only a 1% difference in volume loss between RCP4.5 and RCP8.5 by 2100 CE despite a 1.9°C difference in MAAT—this is a surprising result given the significant temperature difference, which can be attributed to the greater number of high-magnitude precipitation events that occur under RCP8.5 in combination with the small difference in winter temperatures between the two RCPs. Indeed, in the CCCma RCM experiment under RCP4.5, the maximum winter temperature is 1.7°C higher than for the other RCMs, resulting in ablation and rainfall (rather than snowfall) during the winter.

3.3 Climate change and glacier evolution from 2100 CE until 2300 CE

Projections of climate change beyond 2100 CE are more uncertain than those for this century, but do give rise to a clear prognosis for Khumbu Glacier. As there are no regional temperature projections beyond 2100 CE we use global values to continue the simulations into the next century (Table 1). There are no global projections of precipitation beyond 2100 CE and to avoid introducing potentially significant uncertainties to our results by estimating these values, no changes in precipitation are applied beyond 2100 CE.

In all the RCP4.5 experiments, there is little change in glacier volume between 2200 CE and 2300 CE compared with 2100 CE regardless of the RCM forcing used (Table 1 and Fig. 7b). In the NOAA RCP4.5 experiment, the Khumbu Icefall is maintained until 2300 CE and ice continues to flow from the Western Cwm to below 6,000 m so that the glacier remains in contact with the dynamically detached tongue. Therefore, keeping warming within the limit of RCP4.5 will restrict future volume loss to only 26% beyond that already committed to by historical climate change, and Khumbu Glacier would reach a new dynamic equilibrium that maintains a sufficient ice thickness to survive for at least two centuries.

In all the RCP8.5 experiments, substantial glacier loss occurs after 2100 CE and Khumbu Glacier completely decays before 2300 CE. Physical detachment of the debris-covered tongue from the active glacier, whereby this area contains no active glacier ice, occurs around 2140 CE in the NOAA experiment (2070 CE in the CCCma and IPSL experiments) (Fig. 6). We define the glacier to be stagnant when the maximum rate of ice flow is less than 10 m a^{-1}; a conservative estimate of the uncertainty associated with observations of glacier velocities (Dehecq et al., 2019). Accordingly, we consider Khumbu Glacier to no longer be a viable glacier system at the point where there is no ice flow above this value in the entire glacier since there is minimal throughput of ice mass. In the NOAA RCP8.5 experiment, the glacier area is 1.2 km^2 and the mean velocity reduces to 10 m a^{-1} by 2260 CE, such that the glacier is no longer viable as an active system. Glacier breakdown occurs earlier for the CCCma and IPSL RCM experiments because loss of ice volume due to warming is not compensated to the same magnitude by the increase in precipitation projected under RCP8.5 in the NOAA RCM experiment.

4. Discussion

4.1 Uncertainties associated with the climate-glacier modelling approach

The climate-mass balance forcing ensemble was limited in size due to the small number of RCMs available for the CORDEX South Asia region and in this study we considered all of the relevant available forcings. A single RCM was not considered sufficient to represent both present-day climate and potential future climatic extremes but the use of three RCMs allowed the implications of uncertainties in understanding of local climate for glacier evolution to be evaluated. A multi-model mean approach using all the CORDEX South Asia RCMs, widely used elsewhere, was not considered sufficient to represent present-day and future climate conditions in the Khumbu Valley, as this approach gives equal weighting to models irrespective of their performance (Pierce et al., 2009) and does not enable intercomparison of results for future climate conditions.

The differences in simulated glacier change and response time that resulted from the RCMs were at times greater than those resulting from the RCPs due to differences in projections of precipitation. Whilst the three selected RCMs performed relatively well in representing annual precipitation cycles from the six available CORDEX RCMs, we note that this representation was still fairly poor, although substantially improved by quantile mapping. The poor representation of monsoon dynamics in the present-day RCMs highlights an additional uncertainty associated with future precipitation scenarios and that these results should be treated as a set of possible scenarios. The CORDEX CMIP5 and CMIP6 projects only produced dynamically downscaled RCMs for two future emissions scenarios (RCP4.5 and RCP8.5) and as such the implications of other RCPs for glacier evolution could not be assessed. The downscaled future climates were compared with those from other studies using CORDEX results, and showed similar annual and seasonal regional temperature trends strongly linked to the choice of RCP, and similar positive precipitation trends with poor agreement between RCMs (Kaini et al., 2019; Sanjay et al., 2017). The relationship between precipitation and the two future emissions scenarios was less clear than that for air temperatures, because the monsoon-influenced Himalaya shows particularly poor RCM consensus and high levels of uncertainty in future precipitation trends with warming relative to other regions in High Mountain Asia (Sanjay et al., 2017).

Five-year downscaled RCM time slices were chosen to reduce computational expense associated with COSIPY and the integration with the glacier model. To ensure that the five-year periods selected were representative, the preceding decade was used for comparison with the time-slice results, although the use of quantile mapping with 14 years of reference AWS data as the downscaling method will limit the influence of any natural variability by ensuring that the period is not reflecting an extreme phase of natural climate oscillation. This comparison was particularly important for the future time slices where large uncertainties arise between RCMs and there are no observations for evaluation of the downscaled climate or surface mass balance. An experiment was conducted using mid-century (2045–2050 CE) mass balance forcings to investigate any effect on glacier-climate imbalance. This experiment produced near-identical results in 2100 CE to the experiments with no mid-century forcing, because the response time of the simulated glaciers was longer than the 40-year period between the present-day and future time slices, and so the mid-century surface mass balance forcing was not considered necessary in our experiments.

The uncertainties associated with GCM projections increase with time after 2100 CE, particularly under RCP8.5. For example, forecasts of global warming for 2281–2300 CE relative to 1986–2005 CE under RCP8.5 range from 3.0°C to 12.6°C (Collins et al., 2013). In the absence of RCMs that can project changes in precipitation after 2100 CE, precipitation was maintained at the same level for the climate-glacier model simulations beyond 2100 CE. The end-of-century precipitation amount is unlikely to be reflective of the more distant future, and therefore more realistic precipitation projections are required to explore whether the active glacier can be sustained further into the future or will lose ice more rapidly than is found in this study. However, while future precipitation changes may be important for glacier volume change under RCP4.5, we do not expect a sufficient increase in precipitation beyond 2100 CE to compensate for the warming projected under RCP8.5.

The parameterisation of avalanching in the glacier model resulted in increased accumulation along the glacier surface in the Western Cwm and improved the agreement between simulated and observed accumulation rates and distribution. Future work to resolve the impact of low frequency–high magnitude avalanche events on accumulation rates would help to refine this calculation but the contribution of avalanches to glacier accumulation over decadal time scales remains challenging to measure. Our study addresses fine-scale temporal (hourly) and spatial (100 m) glacier surface processes, including avalanching and sublimation, that affect glacier surface mass balance across the elevation range of Khumbu Glacier, but further observations of meteorological and glaciological conditions at the highest elevations would be beneficial, and are needed if micro-scale processes are to be included in glacier models (Brun et al., 2023; Khadka et al., 2021; Mölg et al., 2014; Shaw et al., 2022).

4.2 Comparison of outcomes under RCP4.5 and RCP8.5

Current global greenhouse gas emissions are following the trajectory of the intermediate emissions scenario RCP4.5, while the high emissions scenario RCP8.5 could be described as 'low possibility but high impact' (Pedersen et al., 2020). However, mountain regions are warming more rapidly than the global mean such that a global temperature rise of 1.5°C will lead to 2.1 ± 0.1°C of warming in High Mountain Asia (Kraaijenbrink et al., 2017; Pepin et al., 2022) although the occurrence of elevation-dependent warming above 5,000 m a.s.l. is debated (Gao et al., 2018). High-magnitude precipitation events from winter Westerly disturbances increased by a factor of seven between the present day and 2100 CE in the IPSL RCM under RCP8.5, and could result in net annual glacier mass balances that are less negative than would be the case when solely forced by warming. However, we found no evidence of future increases in precipitation offsetting RCP8.5 warming; net glacier mass balance was strongly negative in all RCP8.5 experiments and insufficient to maintain any actively flowing glacier. Under RCP8.5, glacier mass balance in the monsoon-influenced Himalaya may therefore shift from being driven by accumulation during the monsoon to predominantly during winter. Monsoon precipitation would only result in snow accumulation at the very highest elevations and would be insufficient to maintain flowing glaciers. This outcome is avoidable by limiting anthropogenic warming to within RCP4.5, which, due to the associated increase in precipitation, could sustain nearly two thirds of the current glacier volume until 2100 CE and potentially for two centuries further into the future.

Comparing our results to those for the same glacier from a global modelling study forced by an ensemble of 10 GCMs (Rounce et al., 2023) showed that our experiments project less severe rates of ice volume decline resulting in a smaller amount of loss by 2100 CE (Fig. 8). In our experiments, there is 39% less loss under the RCP4.5 future climate scenario and 32% less under RCP8.5 than in the global study. One difference between these results is that rather than using the global glacier inventory outline to define the glacier margins we consider only the actively flowing glacier and so exclude 20% of the starting glacier volume in the detached tongue. We would expect the two sections of the glacier to evolve along different paths: while the active glacier responds to climate change as projected in our experiments, thick supraglacial debris mantling the detached tongue could allow this ice mass to survive and slowly decay *in situ* for many decades beyond the present day. The decay of the detached tongue may however increase due to erosion of the surface by ice cliffs and supraglacial water bodies that are expanding across the former glacier surface. The dynamically detached debris-covered tongue represents 20% of the present-day glacier volume and contains ice estimated as up to 360 m thick. The mean present-day ablation rate across this section of the glacier simulated in Rowan et al. (2021) is –0.54 m w.e. a^{-1} which can be used to estimate the life expectancy of the debris-covered tongue assuming no input of ice from the active glacier and no change in ablation rate due to thickening of supraglacial debris of the development of ice cliffs and supraglacial ponds. While the thickest part of the detached tongue may survive for ~600 years, the mean life expectancy of this ice mass is 176 ± 148 years from the present day meaning that the former debris-covered tongue will vanish around 2200 CE.

4.3 Impacts of microscale meteorology on glacier change

Sublimation simulated in our study occurred at all elevations with the highest rate of ice loss due to sublimation (–0.12 m w.e. a^{-1}) in the upper reaches of the Khumbu Glacier catchment near to South Col (about 7,495 m a.s.l.) where sublimation dominates ablation with only minor seasonality. Whilst this amount of ice loss by sublimation is not negligible, it is almost half that found in the point-based calculations after adjusting for the different time periods represented by our studies (Matthews et al., 2020), which is likely due to the assumed uniformity of wind speed across the model domain in COSIPY. Future work to improve the calculation of sublimation in distributed surface mass balance calculations for high-elevation glaciers would be valuable. While we have considered the effects of mesoscale meteorology on glacier mass balance, smaller-scale processes operating close to the land surface could also be important. Katabatic winds were suggested to explain a local 15-year decrease in maximum air temperatures and precipitation over glaciers while minimum air temperatures continued to rise (Salerno et al., 2023). However, the impact of micro-scale near-surface cooling on the duration and extent of mesoscale precipitation and accumulation is likely to be minimal and therefore unlikely to significantly affect glacier-wide mass balance (Mott et al., 2020; Shaw et al., 2024). Observations from an AWS on Khumbu Glacier (6,464 m a.s.l.) indicate that surface energy fluxes may be sufficient to cause non-negligible melting of glacier surfaces despite freezing air temperatures (Matthews et al., 2020). Results from an ice core from South Col Glacier (>8,000 m a.s.l.) combined with COSIPY experiments suggested that ablation may also take place at even at the highest elevations (Potocki et al., 2022). However, a subsequent study found no evidence of change, and identified large uncertainties associated with simulating mass balance at these extreme elevations where sub-daily air temperature gradients and the duration of snow cover strongly affect ablation and accumulation (Brun et al., 2023).

4.4 The response of large debris-covered glaciers to climate change

The dynamic response time of large glaciers to climate change is of the order of centuries; for this reason, we start our simulations from the late Holocene (~1 ka) moraine extent when Khumbu Glacier was last considered dynamically stable (Hornsey et al., 2022; Rowan et al., 2015). The relationship between glacier response time and mass balance becomes less important after 2100 CE when the glacier is so small that ice flow has little impact on glacier volume change. Global and regional glacier modelling studies typically start their simulations in the current century (e.g., 2000–2007 CE (Marzeion et al., 2020); 2015 CE in (Rounce et al., 2023)) and a further complication arises from the use of global glacier inventories as a starting point for glacier modelling studies, as such inventories cannot capture the current dynamic state of glaciers that are imbalanced, and include all ice-covered areas rather than identifying only actively flowing ice. However, satellite-derived velocity products could be used identify where ice flow within glacier outlines declines to negligible rates (Dehecq et al., 2019).

The RGI 7.0 inventory for Khumbu Glacier is based on imagery from 1999 CE (RGI 7.0 Consortium, 2023) where the detached debris-covered tongue represents 20% of the glacier volume contained within this outline (Fig. 1c). Simulations that integrated the stagnant tongue into the model domain rather than as part of the flowing ice improved the representation of simulated ice flow compared to observed values, supporting our conclusion that the debris-covered tongue has been dynamically detached from the active glacier for 50–100 years (Rowan et al., 2021). Field observations support the concept of active and stagnant sections co-existing in contact with each other as englacial optical televiewing indicated that thrusting occurs at several sites, denoted by skewed internal debris layers and of basal ice that has been thrust to the glacier surface, near to the active glacier terminus (Fig. 1c) from the direction of Khumbu Icefall (Miles et al., 2021). Our simulations show that development of supraglacial debris at the terminus reduced net volume loss (Fig. 5) but that otherwise the glacier surface is clean (Fig. 4). Therefore, while supraglacial debris sustains about 13% of additional glacier volume compared to a clean-ice surface, after dynamic detachment of debris-covered tongues allow these glaciers to move closer to equilibrium with a rapidly changing climate, the local mass balance gradient is a more important control on glacier change for both clean-ice glaciers and debris-covered Himalayan glaciers.

5. Conclusions

In the monsoon-influenced Himalaya, 85% of the glacier area is located above 5,000 m above sea level and 21% is above 6000 m. Despite these high elevations, Himalayan glaciers are rapidly losing ice in response to recent warming and are projected to shrink by 53% to 70% during this century. However, the impact of future changes in precipitation on glacier loss remains uncertain, because mesoscale meteorology is not often represented in climate-glacier model projections. We explored the effects of future warming in tandem with changes in precipitation by simulating the evolution of Khumbu Glacier in the Everest region of Nepal—a benchmark glacier in the monsoon-influenced Nepal Himalaya—using mesoscale climate-glacier modelling forced by downscaled Regional Climate Model outputs. Historical warming commits Khumbu Glacier to loss of 10–23% of the total ice volume by 2100 CE. While warming due to intermediate future greenhouse gas emissions (RCP4.5) will lead to glacier volume loss of 70% by 2100 CE, the projected concurrent increase in precipitation amount will offset 34% of this and so reduce glacier loss by about a half. However, high future emissions (RCP8.5) will not be compensated by changes in precipitation amount but will instead result in substantial ablation above 6,000 m and cause Khumbu Glacier to vanish by 2160–2260 CE. Our results indicate that the net mass balance of Khumbu Glacier could be close to zero in 2100 CE under RCP4.5 and therefore, if climate change is limited to this intermediate emissions scenario, Khumbu Glacier will recede to the base of the icefall with insignificant further change in glacier volume beyond this point. In this scenario, Khumbu Glacier has a similar extent in 2100 CE to the active section of the present-day glacier, and represents at least one example of how monsoon-influenced Himalayan glaciers could persist into the future if global efforts are sufficient to mitigate anthropogenic climate change.

Code availability

The COSIPY surface energy balance model is available from the original publication describing this model (Sauter et al., 2020). The version of the glacier model used in this study is available from Zenodo (Rowan, 2024).

Data availability

Daily data from the Coordinated Regional Downscaling Experiment (CORDEX) South Asia domain were downloaded from the Indian Institute of Tropical Meteorology website (http://cccr.tropmet.res.in/home/cordexsa_about.jsp) for the grid box nearest to Khumbu Glacier (27.9065°N, 86.4353°E). Incoming shortwave and longwave radiation components were downloaded from the ESGF portal (https://esgf-ui.ceda.ac.uk/cog/projects/cordex-ceda/). 14 years of meteorological observations were derived from the two Pyramid AWS at 5,050 m a.s.l and at 5,035 m a.s.l (SHARE network Ev-K2-CNR; https://www.evk2cnr.org) and the West Changri Nup glacier AWS at 5,363 m a.s.l (GlacioClim: https://glacioclim.osug.fr/).

Author contributions

Conceptualisation: DJQ, ANR, AVR
Data curation: ASD, ANR, AVR
Formal analysis: ASD, ANR, AVR
Funding acquisition: DJQ, ANR, AVR
Investigation: ASD
Methodology: ASD, ANR, AVR, VKP
Project administration: DJQ, ANR
Resources: DJQ, ANR
Software: AVR, VKP
Supervision: DJQ, ANR, AVR
Validation: ASD, AVR
Visualisation: ASD, AVR
Writing – original draft preparation: ASD, AVR, DJQ, ANR, VKP
Writing – review and editing: ASD, AVR, DJQ, ANR, VKP

Competing interests

The authors declare that they have no conflict of interest.

Acknowledgements

Tobias Sauter and Anselm Arndt are thanked for support in using COSIPY. We thank Patrick Wagnon for sharing the Pyramid and Changri Nup Glacier automatic weather station data. We thank David Rounce for sharing global glacier model results for Khumbu Glacier from Rounce et al. (2023). Some of the simulations presented were performed on resources provided by Sigma2, the National Infrastructure for High-Performance Computing and Data Storage in Norway.

Financial support

ASD was supported by the Priestley International Centre for Climate at the University of Leeds, and a University of Leeds Anniversary Research Scholarship. AVR was supported by a Royal Society Dorothy Hodgkin Research Fellowship (DHF\R1\201113).

References

Altena, B. and Kääb, A.: Ensemble matching of repeat satellite images applied to measure fast-changing ice flow, verified with mountain climber trajectories on Khumbu icefall, Mount Everest, J. Glaciol., 66, 905–915, https://doi.org/10.1017/jog.2020.66, 2020.

Anderson, L. S. and Anderson, R. S.: Modeling debris-covered glaciers: response to steady debris deposition, The Cryosphere, 10, 1105–1124, https://doi.org/10.5194/tc-10-1105-2016, 2016.

Bartlett, O. T., Ng, F. S. L., and Rowan, A. V.: Morphology and evolution of supraglacial hummocks on debris-covered Himalayan glaciers, Earth Surf. Process. Landforms, 46, 525–539, https://doi.org/10.1002/esp.5043, 2021.

Benn, D. I. and Lehmkuhl, F.: Mass balance and equilibrium-line altitudes of glaciers in high-mountain environments, Quaternary International, 65–66, 15–29, https://doi.org/10.1016/S1040-6182(99)00034-8, 2000.

Benn, D. I. and Owen, L. A.: The role of the Indian summer monsoon and the mid-latitude westerlies in Himalayan glaciation: review and speculative discussion, Journal of the Geological Society, 155, 353–363, https://doi.org/10.1144/gsjgs.155.2.0353, 1998.

Bonekamp, P. N. J., Wanders, N., Wiel, K., Lutz, A. F., and Immerzeel, W. W.: Using large ensemble modelling to derive future changes in mountain specific climate indicators in a 2 and 3°C warmer world in High Mountain Asia, Int J Climatol, 41, https://doi.org/10.1002/joc.6742, 2021.

Bookhagen, B. and Burbank, D. W.: Topography, relief, and TRMM-derived rainfall variations along the Himalaya, Geophys. Res. Lett., 33, L08405, https://doi.org/10.1029/2006GL026037, 2006.

Brun, F., King, O., Réveillet, M., Amory, C., Planchot, A., Berthier, E., Dehecq, A., Bolch, T., Fourteau, K., Brondex, J., Dumont, M., Mayer, C., Leinss, S., Hugonnet, R., and Wagnon, P.: Everest South Col Glacier did not thin during the period 1984–2017, The Cryosphere, 17, 3251–3268, https://doi.org/10.5194/tc-17-3251-2023, 2023.

Collins, M., Knutti, R., and Arblaster, J.: Long-term Climate Change: Projections, Commitments and Irreversibility. In: Climate Change 2013: The Physical Science Basis. Contribution of Working Group I to the Fifth Assessment Report of the Intergovernmental Panel on Climate Change [Stocker, T.F., D. Qin, G.-K. Plattner, M. Tignor, S.K. Allen, J. Boschung, A. Nauels, Y. Xia, V. Bex and P.M. Midgley (eds.)]. Cambridge University Press, Cambridge, United Kingdom and New York, NY, USA,, 1–108., 2013.

Compagno, L., Huss, M., Miles, E. S., McCarthy, M. J., Zekollari, H., Dehecq, A., Pellicciotti, F., and Farinotti, D.: Modelling supraglacial debris-cover evolution from the single-glacier to the regional scale: an application to High Mountain Asia, The Cryosphere, 16, 1697–1718, https://doi.org/10.5194/tc-16-1697-2022, 2022.

Dehecq, A., Gourmelen, N., Gardner, A. S., Brun, F., Goldberg, D., Nienow, P. W., Berthier, E., Vincent, C., Wagnon, P., and Trouvé, E.: Twenty-first century glacier slowdown driven by mass loss in High Mountain Asia, Nature Geosci, 12, 22–27, https://doi.org/10.1038/s41561-018-0271-9, 2019.

Egholm, D. L., Knudsen, M. F., Clark, C. D., and Lesemann, J. E.: Modeling the flow of glaciers in steep terrains: The integrated second-order shallow ice approximation (iSOSIA): MODELING GLACIERS WHERE TOPOGRAPHY IS STEEP, J. Geophys. Res., 116, https://doi.org/10.1029/2010JF001900, 2011.

Farinotti, D., Huss, M., Fürst, J. J., Landmann, J., Machguth, H., Maussion, F., and Pandit, A.: A consensus estimate for the ice thickness distribution of all glaciers on Earth, Nat. Geosci., 12, 168–173, https://doi.org/10.1038/s41561-019-0300-3, 2019.

Farr, T. G., Rosen, P. A., Caro, E., Crippen, R., Duren, R., Hensley, S., Kobrick, M., Paller, M., Rodriguez, E., Roth, L., Seal, D., Shaffer, S., Shimada, J., Umland, J., Werner, M., Oskin, M., Burbank, D., and Alsdorf, D.: The Shuttle Radar Topography Mission, Reviews of Geophysics, 45, 2005RG000183, https://doi.org/10.1029/2005RG000183, 2007.

Ferguson, J. and Vieli, A.: Modelling steady states and the transient response of debris-coveredglaciers, https://doi.org/10.5194/tc-2020-228, 2020.

Förster, K., Hanzer, F., Winter, B., Marke, T., and Strasser, U.: An open-source MEteoroLOgical observation time series DISaggregation Tool (MELODIST v0.1.1), Geosci. Model Dev., 9, 2315–2333, https://doi.org/10.5194/gmd-9-2315-2016, 2016.

Gades, A., Conway, H., Nereson, N., Naito, N., and Kadota, T.: Radio echo-sounding through supraglacial debris on Lirung and Khumbu Glaciers, Nepal Himalayas, Debris-Covered Glaciers (Proceedings of a workshop held at Seattle, Washington, USA, September 2000). IAHS, 264, 13–22, 2000.

Gao, Y., Chen, F., Lettenmaier, D. P., Xu, J., Xiao, L., and Li, X.: Does elevation-dependent warming hold true above 5000 m elevation? Lessons from the Tibetan Plateau, npj Clim Atmos Sci, 1, 19, https://doi.org/10.1038/s41612-018-0030-z, 2018.

Herreid, S. and Pellicciotti, F.: The state of rock debris covering Earth's glaciers, Nat. Geosci., 13, 621–627, https://doi.org/10.1038/s41561-020-0615-0, 2020.

Hornsey, J., Rowan, A. V., Kirkbride, M. P., Livingstone, S. J., Fabel, D., Rodes, A., Quincey, D. J., Hubbard, B., and Jomelli, V.: Be-10 Dating of Ice-Marginal Moraines in the Khumbu Valley, Nepal, Central Himalaya, Reveals the Response of Monsoon-Influenced Glaciers to Holocene Climate Change, JGR Earth Surface, 127, https://doi.org/10.1029/2022JF006645, 2022.

Huintjes, E., Neckel, N., Hochschild, V., and Schneider, C.: Surface energy and mass balance at Purogangri ice cap, central Tibetan Plateau, 2001–2011, J. Glaciol., 61, 1048–1060, https://doi.org/10.3189/2015JoG15J056, 2015.

Immerzeel, W. W., van Beek, L. P. H., Konz, M., Shrestha, A. B., and Bierkens, M. F. P.: Hydrological response to climate change in a glacierized catchment in the Himalayas, Climatic Change, 110, 721–736, https://doi.org/10.1007/s10584-011-0143-4, 2012.

Jouvet, G., Huss, M., Funk, M., and Blatter, H.: Modelling the retreat of Grosser Aletschgletscher, Switzerland, in a changing climate, J. Glaciol., 57, 1033–1045, https://doi.org/10.3189/002214311798843359, 2011.

Katzenberger, A., Schewe, J., Pongratz, J., and Levermann, A.: Robust increase of Indian monsoon rainfall and its variability under future warming in CMIP6 models, Earth Syst. Dynam., 12, 367–386, https://doi.org/10.5194/esd-12-367-2021, 2021.

Khadka, A., Matthews, T., Perry, L. B., Koch, I., Wagnon, P., Shrestha, D., Sherpa, T. C., Aryal, D., Tait, A., Sherpa, T. G., Tuladhar, S., Baidya, S. K., Elvin, S., Elmore, A. C., Gajurel, A., and Mayewski, P. A.: Weather on MOUNT EVEREST during the 2019 summer MONSOON, Weather, 76, 205–207, https://doi.org/10.1002/wea.3931, 2021.

King, O., Bhattacharya, A., Ghuffar, S., Tait, A., Guilford, S., Elmore, A. C., and Bolch, T.: Six Decades of Glacier Mass Changes around Mt. Everest Are Revealed by Historical and Contemporary Images, One Earth, 3, 608–620, https://doi.org/10.1016/j.oneear.2020.10.019, 2020.

Kraaijenbrink, P. D. A., Bierkens, M. F. P., Lutz, A. F., and Immerzeel, W. W.: Impact of a global temperature rise of 1.5 degrees Celsius on Asia's glaciers, Nature, 549, 257–260, https://doi.org/10.1038/nature23878, 2017.

Marzeion, B., Hock, R., Anderson, B., Bliss, A., Champollion, N., Fujita, K., Huss, M., Immerzeel, W. W., Kraaijenbrink, P., Malles, J., Maussion, F., Radić, V., Rounce, D. R., Sakai, A., Shannon, S., Van De Wal, R., and Zekollari, H.: Partitioning the Uncertainty of Ensemble Projections of Global Glacier Mass Change, Earth's Future, 8, e2019EF001470, https://doi.org/10.1029/2019EF001470, 2020.

Matthews, T., Perry, L. B., Koch, I., Aryal, D., Khadka, A., Shrestha, D., Abernathy, K., Elmore, A. C., Seimon, A., Tait, A., Elvin, S., Tuladhar, S., Baidya, S. K., Potocki, M., Birkel, S. D., Kang, S., Sherpa, T. C., Gajurel, A., and Mayewski, P. A.: Going to Extremes: Installing the World's Highest Weather Stations on Mount Everest, Bulletin of the American Meteorological Society, 101, E1870–E1890, https://doi.org/10.1175/BAMS-D-19-0198.1, 2020.

Maurer, J. M., Schaefer, J. M., Rupper, S., and Corley, A.: Acceleration of ice loss across the Himalayas over the past 40 years, Sci. Adv., 5, eaav7266, https://doi.org/10.1126/sciadv.aav7266, 2019.

Miles, E. S., Willis, I., Buri, P., Steiner, J. F., Arnold, N. S., and Pellicciotti, F.: Surface Pond Energy Absorption Across Four Himalayan Glaciers Accounts for 1/8 of Total Catchment Ice Loss, Geophys. Res. Lett., 45, https://doi.org/10.1029/2018GL079678, 2018a.

Miles, K. E., Hubbard, B., Quincey, D. J., Miles, E. S., Sherpa, T. C., Rowan, A. V., and Doyle, S. H.: Polythermal structure of a Himalayan debris-covered glacier revealed by borehole thermometry, Sci Rep, 8, 16825, https://doi.org/10.1038/s41598-018-34327-5, 2018b.

Miles, K. E., Hubbard, B., Miles, E. S., Quincey, D. J., Rowan, A. V., Kirkbride, M., and Hornsey, J.: Continuous borehole optical televiewing reveals variable englacial debris concentrations at Khumbu Glacier, Nepal, Commun Earth Environ, 2, 12, https://doi.org/10.1038/s43247-020-00070-x, 2021.

Mölg, T., Maussion, F., and Scherer, D.: Mid-latitude westerlies as a driver of glacier variability in monsoonal High Asia, Nature Clim Change, 4, 68–73, https://doi.org/10.1038/nclimate2055, 2014.

Mott, R., Stiperski, I., and Nicholson, L.: Spatio-temporal flow variations driving heat exchange processes at a mountain glacier, The Cryosphere, 14, 4699–4718, https://doi.org/10.5194/tc-14-4699-2020, 2020.

Nakawo, M.: PROCESSES WHICH DISTRIBUTE SUPRAGLACIAL DEBRIS ON THE KHUMBU GLACIER, NEPAL HIMALAYA, 3, 1986.

Nicholson, L., Wirbel, A., Mayer, C., and Lambrecht, A.: The Challenge of Non-Stationary Feedbacks in Modeling the Response of Debris-Covered Glaciers to Climate Forcing, Front. Earth Sci., 9, 662695, https://doi.org/10.3389/feart.2021.662695, 2021.

Owen, L. A., Robinson, R., Benn, D. I., Finkel, R. C., Davis, N. K., Yi, C., Putkonen, J., Li, D., and Murray, A. S.: Quaternary glaciation of Mount Everest, Quaternary Science Reviews, 28, 1412–1433, https://doi.org/10.1016/j.quascirev.2009.02.010, 2009.

Pedersen, J. S. T., Van Vuuren, D. P., Aparício, B. A., Swart, R., Gupta, J., and Santos, F. D.: Variability in historical emissions trends suggests a need for a wide range of global scenarios and regional analyses, Commun Earth Environ, 1, 41, https://doi.org/10.1038/s43247-020-00045-y, 2020.

Pellicciotti, F., Stephan, C., Miles, E., Herreid, S., Immerzeel, W. W., and Bolch, T.: Mass-balance changes of the debris-covered glaciers in the Langtang Himal, Nepal, from 1974 to 1999, J. Glaciol., 61, 373–386, https://doi.org/10.3189/2015JoG13J237, 2015.

Pepin, N. C., Arnone, E., Gobiet, A., Haslinger, K., Kotlarski, S., Notarnicola, C., Palazzi, E., Seibert, P., Serafin, S., Schöner, W., Terzago, S., Thornton, J. M., Vuille, M., and Adler, C.: Climate Changes and Their Elevational Patterns in the Mountains of the World, Reviews of Geophysics, 60, https://doi.org/10.1029/2020RG000730, 2022.

Pierce, D. W., Barnett, T. P., Santer, B. D., and Gleckler, P. J.: Selecting global climate models for regional climate change studies, Proc. Natl. Acad. Sci. U.S.A., 106, 8441–8446, https://doi.org/10.1073/pnas.0900094106, 2009.

Potocki, M., Mayewski, P. A., Matthews, T., Perry, L. B., Schwikowski, M., Tait, A. M., Korotkikh, E., Clifford, H., Kang, S., Sherpa, T. C., Singh, P. K., Koch, I., and Birkel, S.: Mt. Everest's highest glacier is a sentinel for accelerating ice loss, npj Clim Atmos Sci, 5, 7, https://doi.org/10.1038/s41612-022-00230-0, 2022.

Pritchard, H. D.: Asia's shrinking glaciers protect large populations from drought stress, Nature, 569, 649–654, https://doi.org/10.1038/s41586-019-1240-1, 2019.

Quincey, D. J., Luckman, A., and Benn, D.: Quantification of Everest region glacier velocities between 1992 and 2002, using satellite radar interferometry and feature tracking, J. Glaciol., 55, 596–606, https://doi.org/10.3189/002214309789470987, 2009.

Ragettli, S., Immerzeel, W. W., and Pellicciotti, F.: Contrasting climate change impact on river flows from high-altitude catchments in the Himalayan and Andes Mountains, Proc Natl Acad Sci USA, 113, 9222–9227, https://doi.org/10.1073/pnas.1606526113, 2016.

RGI 7.0 Consortium: A Dataset of Global Glacier Outlines, Version 7.0. Boulder, Colorado USA. NSIDC: National Snow and Ice Data Center, https://doi.org/10.5067/f6jmovy5navz, 2023.

Roering, J. J., Kirchner, J. W., and Dietrich, W. E.: Evidence for nonlinear, diffusive sediment transport on hillslopes and implications for landscape morphology, Water Resources Research, 35, 853–870, https://doi.org/10.1029/1998WR900090, 1999.

Rounce, D. R., Hock, R., Maussion, F., Hugonnet, R., Kochtitzky, W., Huss, M., Berthier, E., Brinkerhoff, D., Compagno, L., Copland, L., Farinotti, D., Menounos, B., and McNabb, R. W.: Global glacier change in the 21st century: Every increase in temperature matters, Science, 379, 78–83, https://doi.org/10.1126/science.abo1324, 2023.

Rowan, A. V.: The 'Little Ice Age' in the Himalaya: A review of glacier advance driven by Northern Hemisphere temperature change, The Holocene, 27, 292–308, https://doi.org/10.1177/0959683616658530, 2017.

Rowan, A. V., Egholm, D. L., Quincey, D. J., and Glasser, N. F.: Modelling the feedbacks between mass balance, ice flow and debris transport to predict the response to climate change of debris-covered glaciers in the Himalaya, Earth and Planetary Science Letters, 430, 427–438, https://doi.org/10.1016/j.epsl.2015.09.004, 2015.

Rowan, A. V., Egholm, D. L., Quincey, D. J., Hubbard, B., King, O., Miles, E. S., Miles, K. E., and Hornsey, J.: The Role of Differential Ablation and Dynamic Detachment in Driving Accelerating

Mass Loss From a Debris-Covered Himalayan Glacier, J. Geophys. Res. Earth Surf., 126, https://doi.org/10.1029/2020JF005761, 2021.

Salerno, F., Guyennon, N., Yang, K., Shaw, T. E., Lin, C., Colombo, N., Romano, E., Gruber, S., Bolch, T., Alessandri, A., Cristofanelli, P., Putero, D., Diolaiuti, G., Tartari, G., Verza, G., Thakuri, S., Balsamo, G., Miles, E. S., and Pellicciotti, F.: Local cooling and drying induced by Himalayan glaciers under global warming, Nat. Geosci., 16, 1120–1127, https://doi.org/10.1038/s41561-023-01331-y, 2023.

Sanjay, J., Krishnan, R., Shrestha, A. B., Rajbhandari, R., and Ren, G.-Y.: Downscaled climate change projections for the Hindu Kush Himalayan region using CORDEX South Asia regional climate models, Advances in Climate Change Research, 8, 185–198, https://doi.org/10.1016/j.accre.2017.08.003, 2017.

Sauter, T., Arndt, A., and Schneider, C.: COSIPY v1.3 – an open-source coupled snowpack and ice surface energy and mass balance model, Geosci. Model Dev., 13, 5645–5662, https://doi.org/10.5194/gmd-13-5645-2020, 2020.

Shaw, T. E., Miles, E. S., Chen, D., Jouberton, A., Kneib, M., Fugger, S., Ou, T., Lai, H.-W., Fujita, K., Yang, W., Fatichi, S., and Pellicciotti, F.: Multi-decadal monsoon characteristics and glacier response in High Mountain Asia, Environ. Res. Lett., 17, 104001, https://doi.org/10.1088/1748-9326/ac9008, 2022.

Shaw, T. E., Buri, P., McCarthy, M., Miles, E. S., and Pellicciotti, F.: Local Controls on Near-Surface Glacier Cooling Under Warm Atmospheric Conditions, JGR Atmospheres, 129, e2023JD040214, https://doi.org/10.1029/2023JD040214, 2024.

Shea, J. M., Immerzeel, W. W., Wagnon, P., Vincent, C., and Bajracharya, S.: Modelling glacier change in the Everest region, Nepal Himalaya, The Cryosphere, 9, 1105–1128, https://doi.org/10.5194/tc-9-1105-2015, 2015.

Strickland, R. M., Covington, M. D., Gulley, J. D., Kayastha, R. B., and Blackstock, J. M.: Englacial Drainage Drives Positive Feedback Depression Growth on the Debris-Covered Ngozumpa Glacier, Nepal, Geophysical Research Letters, 50, e2023GL104389, https://doi.org/10.1029/2023GL104389, 2023.

Vacco, D. A., Alley, R. B., and Pollard, D.: Glacial advance and stagnation caused by rock avalanches, Earth and Planetary Science Letters, 294, 123–130, https://doi.org/10.1016/j.epsl.2010.03.019, 2010.

Watson, C. S., Quincey, D. J., Smith, M. W., Carrivick, J. L., Rowan, A. V., and James, M. R.: Quantifying ice cliff evolution with multi-temporal point clouds on the debris-covered Khumbu Glacier, Nepal, J. Glaciol., 63, 823–837, https://doi.org/10.1017/jog.2017.47, 2017.

Wirbel, A., Jarosch, A. H., and Nicholson, L.: Modelling debris transport within glaciers by advection in a full-Stokes ice flow model, The Cryosphere, 12, 189–204, https://doi.org/10.5194/tc-12-189-2018, 2018.

Zekollari, H., Huss, M., Farinotti, D., and Lhermitte, S.: Ice-Dynamical Glacier Evolution Modeling—A Review, Reviews of Geophysics, 60, https://doi.org/10.1029/2021RG000754, 2022.

Table and caption

Table 1. Regional Climate Models (RCMs) chosen for this study and details of the Global Circulation Models (GCMs) from which these are derived. The NOAA RCM that was considered most representative of conditions in the Everest region. The temperature forcings used to project climate change beyond 2100 CE are global values (they are simply included against each of the RCMs for ease comparing with 2100 temperature change) and include no change in precipitation after 2100 CE.

CORDEX South Asia regional climate model	Driving CMIP5 global climate model	CMIP5 modelling centre	RCM name in this study	Future precipitation scenario (qualitative)	2100 CE mean temperature change from present day (°C)		2200 CE mean temperature change from 2100 CE (°C)		2300 CE mean temperature change from 2100 CE (°C) */2200CE*	
					RCP 4.5	RCP 8.5	RCP 4.5	RCP 8.5	RCP 4.5	RCP 8.5
ITTM-RegCM4	NOAA-GFDL-GFDL-ESM2M	National Oceanic and Atmospheric Administration (NOAA), USA	NOAA	Wet	1.4	3.8	0.5	2.8	0.7 */0.2*	4.1 */1.3*
IITM-RegCM4	CCCma-CanESM2	Canadian Centre for Climate Modelling and Analysis (CCCma), Canada	CCCma	Moderate	2.2	4.1	0.5	2.8	0.7	4.1
IITM-RegCM4	IPSL-CMSA-LR	Institue Pierre-Simon Laplace (IPSL), France	IPSL	Dry	1.6	3.8	0.5	2.8	0.7	4.1

Figures and captions

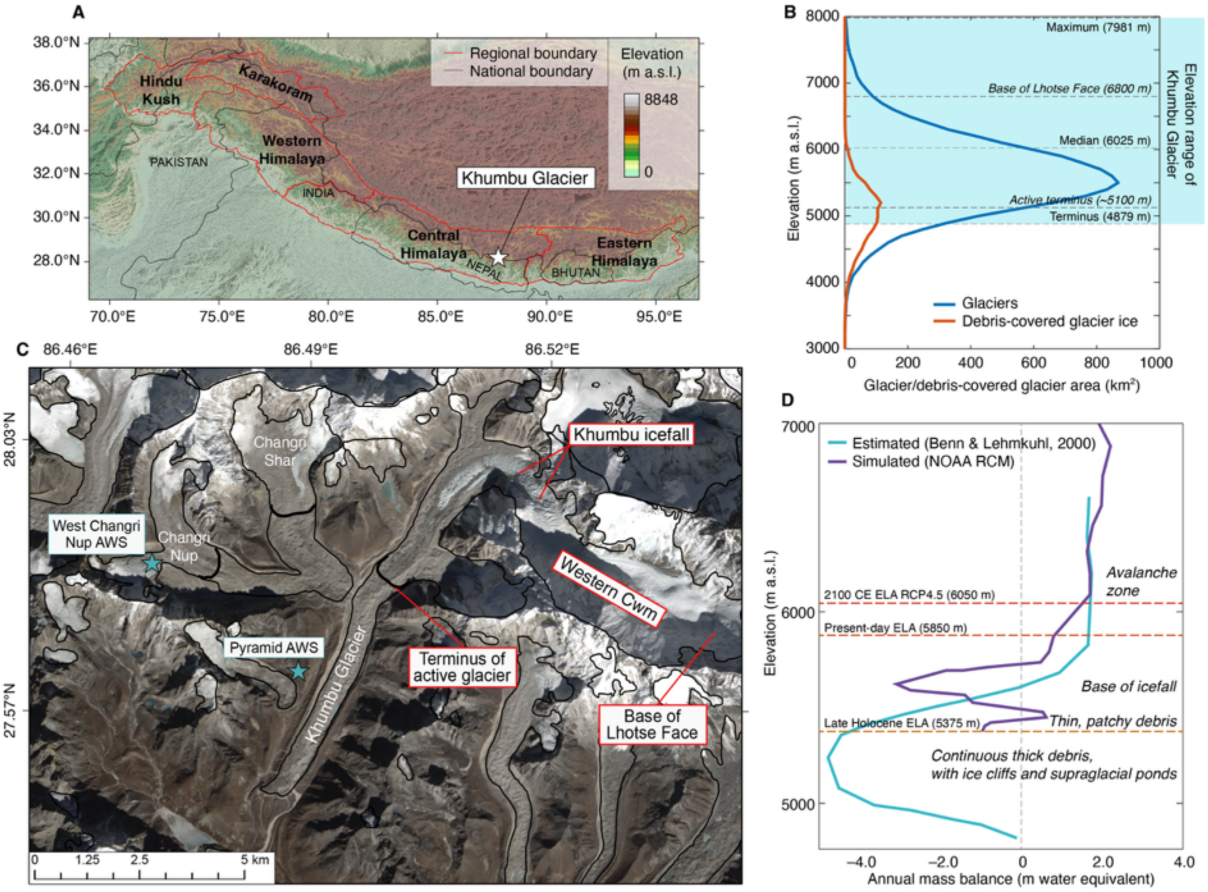

Figure 1: Khumbu Glacier location and context. (a) Location map of High Mountain Asia showing the location of the monsoon-influenced Central and Eastern Himalaya and Khumbu Glacier. (b) hypsometry of glaciers and debris-covered glacier ice in the Central and Eastern Himalaya compared with the elevations of Khumbu Glacier. (c) Satellite image of Khumbu Glacier showing the glacier outline from the RGI database (black line) that is equivalent to the late Holocene (~1 ka) glacier extent identified from ice-marginal moraines, the extent of supraglacial debris, location of the Khumbu Icefall, the extent of active ice flow inferred from observations of glacier velocity, and location of the automatic weather stations used for RCM downscaling (blue stars). (d) Estimated mass balance gradient for debris-covered glaciers in the Everest region (Benn and Lehmkuhl, 2000) compared with the glacier mass balance gradient simulated using the NOAA RCM and showing change in the equilibrium line altitude (ELA) of Khumbu Glacier in the historical and future simulations for the NOAA RCM RCP4.5 experiment.

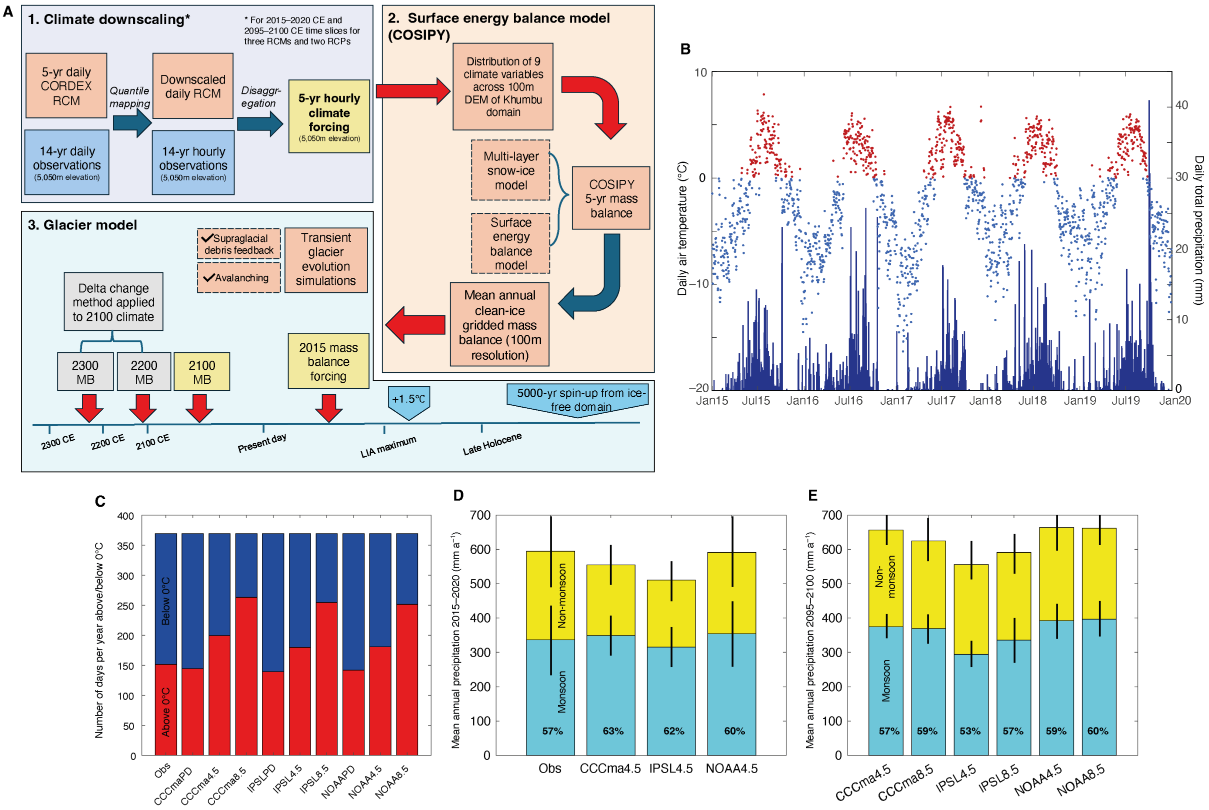

Figure 2: Climate-glacier model experimental design and evaluation of RCM downscaling. (a) Schematic diagram of the climate-glacier modelling approach showing the methods used for downscaling through quantile mapping and disaggregation of climate data. Note that this process does not apply to the post-2100 CE climate forcings which are subject to delta change. Surface energy balance modelling using COSIPY includes the pre-processing stage of meteorological distribution across the Khumbu domain, which is repeated for each RCM in the 2015–2020 CE climates and for the three RCMs and two RCPs for the 2095–2100 CE climates. The simulated mass balance is then used to force the glacier evolution model. (b) Daily mean temperature and daily total precipitation from the NOAA RCM for the present day (2015–2020 CE) following downscaling using quantile mapping with air temperature categorised into above freezing (red) and below freezing (blue). (c) Proportion of air temperatures above and below freezing for the present day for each RCM and RCP for the downscaled daily data compared with observations. (d) Annual precipitation totals for non-monsoon and monsoon with standard deviation between selected years shown by black bars for the downscaled daily data compared with observations. (e) Future (2095–2100 CE) time-slice annual precipitation totals for non-monsoon and monsoon months with standard deviation between selected years shown by black bars. In (d) and (e) the percentage of the total annual precipitation occurring during the monsoon is indicated by the value in bold text. (Obs = meteorological observations from AWS).

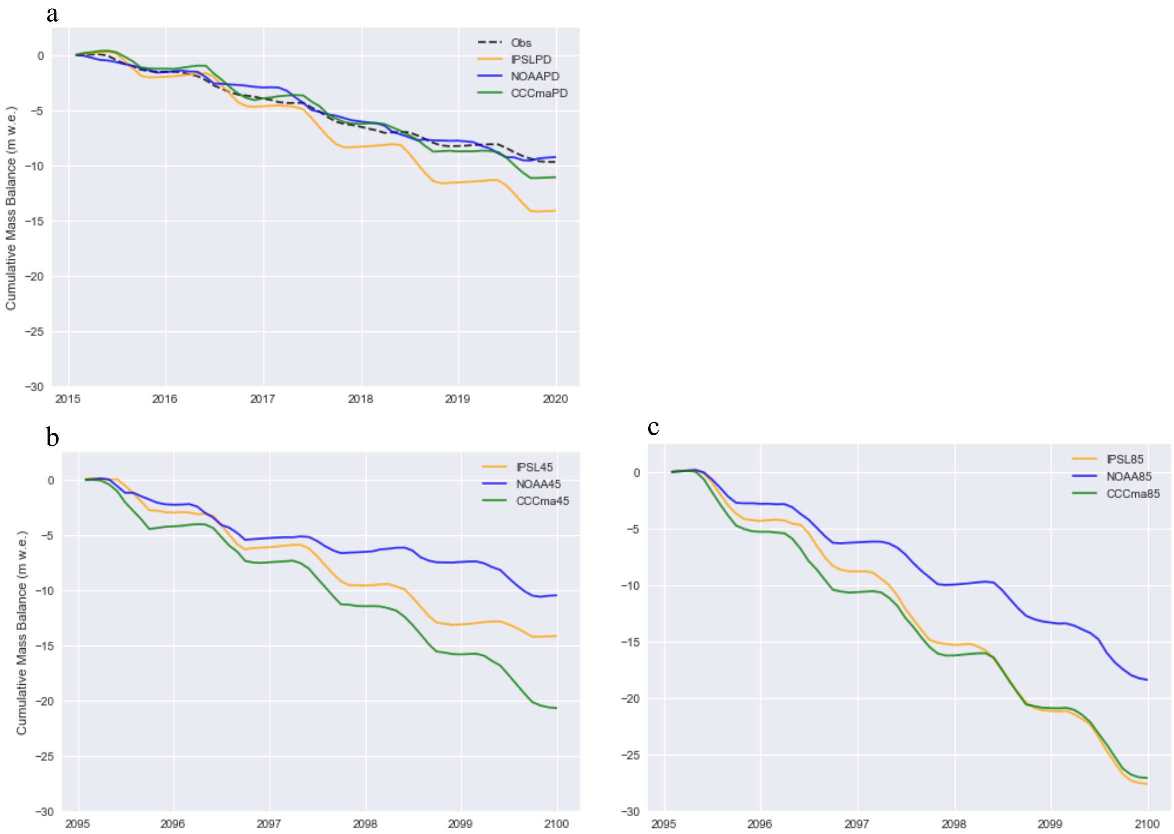

Figure 3: Spatially averaged cumulative clean-ice mass balance with clear seasonality for (a) the present day time-slice including the mass balance forced by the observations used for downscaling, and the end-of-century time-slice under (b) RCP4.5 and (c) RCP8.5. The low annual glacier-wide mass balance values shown here are the result of the extent of the model domain used to force the glacier model that includes the larger catchment beyond the glacier margins and therefore contains a higher proportion of lower elevations than those of the glacier itself. However the similar mass balance results for simulations forced by NOAA RCM and observations can be clearly seen (a), and the differences between the three RCMs is apparent in all time-slices (a-c).

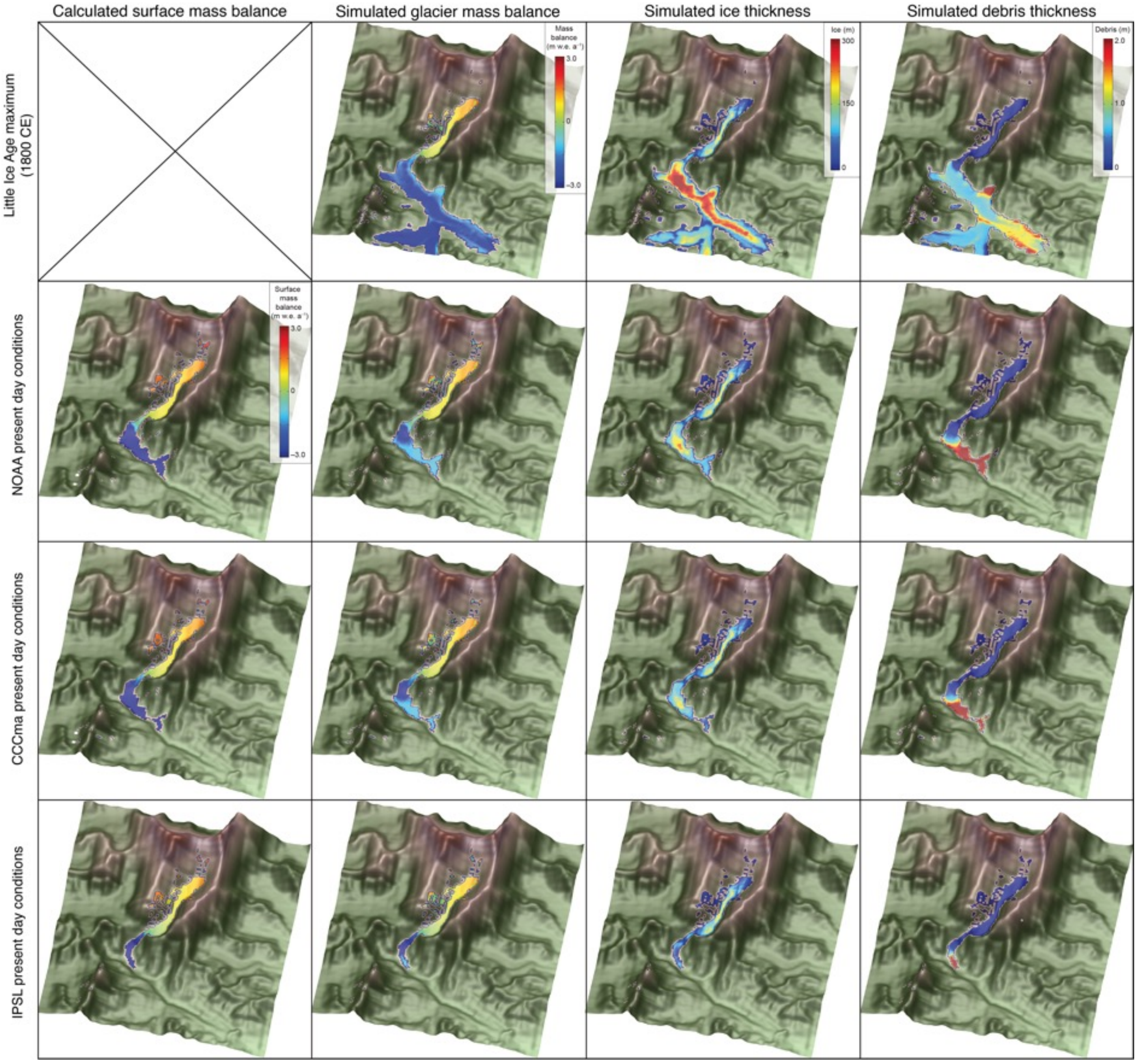

Figure 4. Glacier model sensitivity to surface energy and mass balance forcing, showing Little Ice Age (~1800 CE) glacier mass balance, ice thickness and debris thickness. Present-day results for surface mass balance calculated using each RCM with COSIPY showing glacier mass balance calculated using the same climate forcing following integration with the glacier model, simulated ice thickness, and simulated debris thickness.

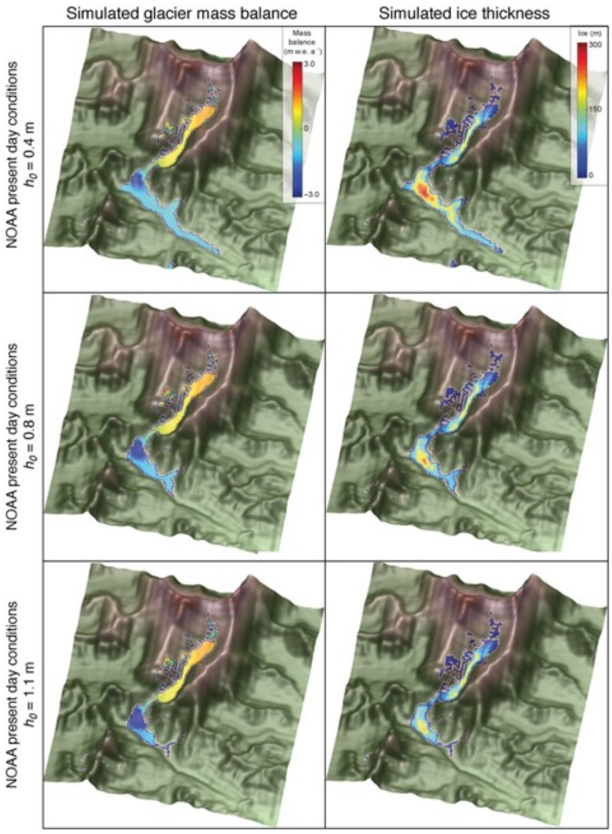

Figure 5. Glacier mass balance and ice thickness simulated using the NOAA RCM climate forcing and the resulting simulated ice thickness for h_0 values of 0.4 m, 0.8 m, and 1.1 m where h_0 is a constant in Equation(1) representing the characteristic debris thickness at which the reduction in ablation due to insulation by supraglacial debris is 50% of the value for an equivalent clean-ice surface (Anderson and Anderson, 2016; Rowan et al., 2021).

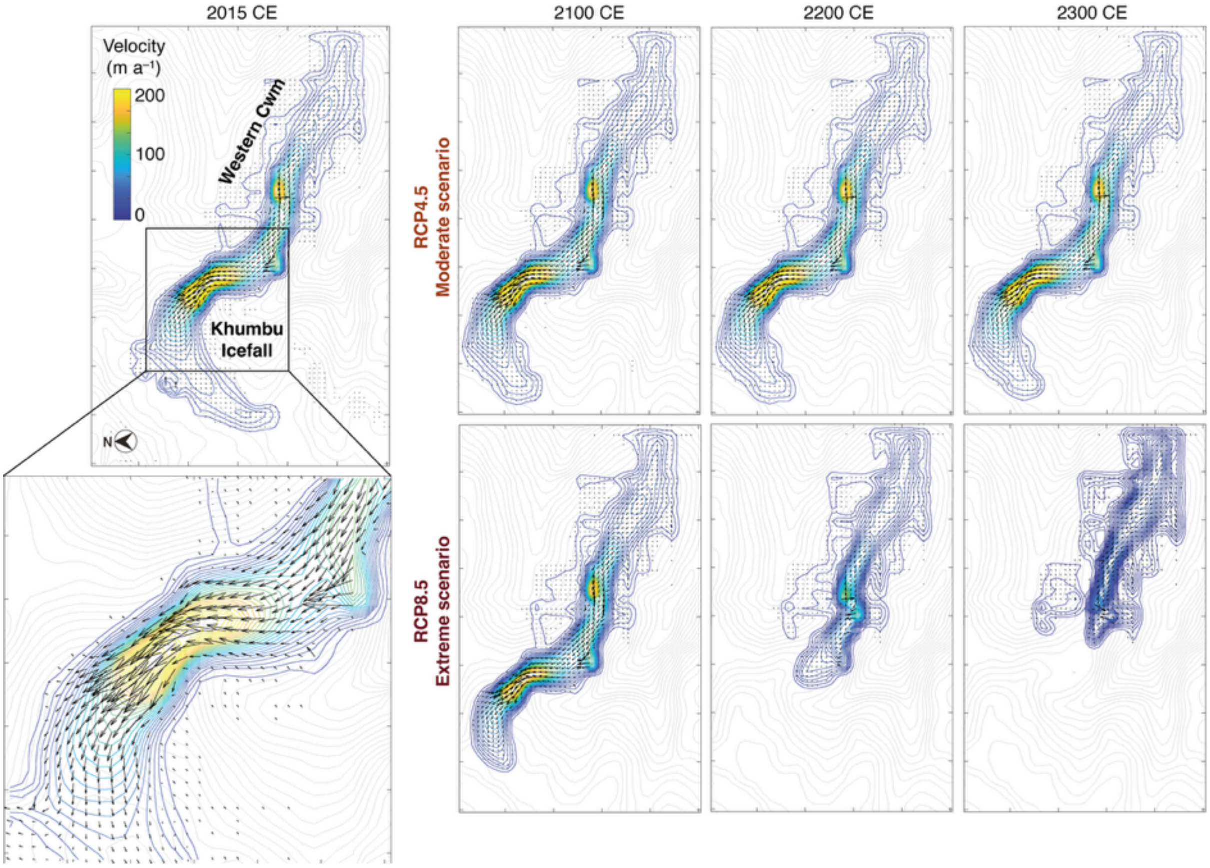

Figure 6. Simulated ice flow for Khumbu Glacier. Velocity-vector maps showing simulated ice flow magnitude and direction from the present day (2015–2020 CE) until 2300 CE under RCP4.5 and RCP8.5 using the downscaled NOAA climate forcing and a value for h_0 of 0.8 m where h_0 is a constant in Equation(1) representing the characteristic debris thickness at which the reduction in ablation due to insulation by supraglacial debris is 50% of the value for an equivalent clean-ice surface (Anderson and Anderson, 2016; Rowan et al., 2021). Simulated ice flow speed is shown as colour shading with blue contours, and the bed topography is shown by grey contours. The outermost contour in each plot represents the slowest ice flow close to the glacier margins with depth-integrated velocities of 5–10 m a^{-1}. Note that rapid flow across the Western Cwm indicated by one arrow shows the effects of avalanching rather than sustained glacier flow.

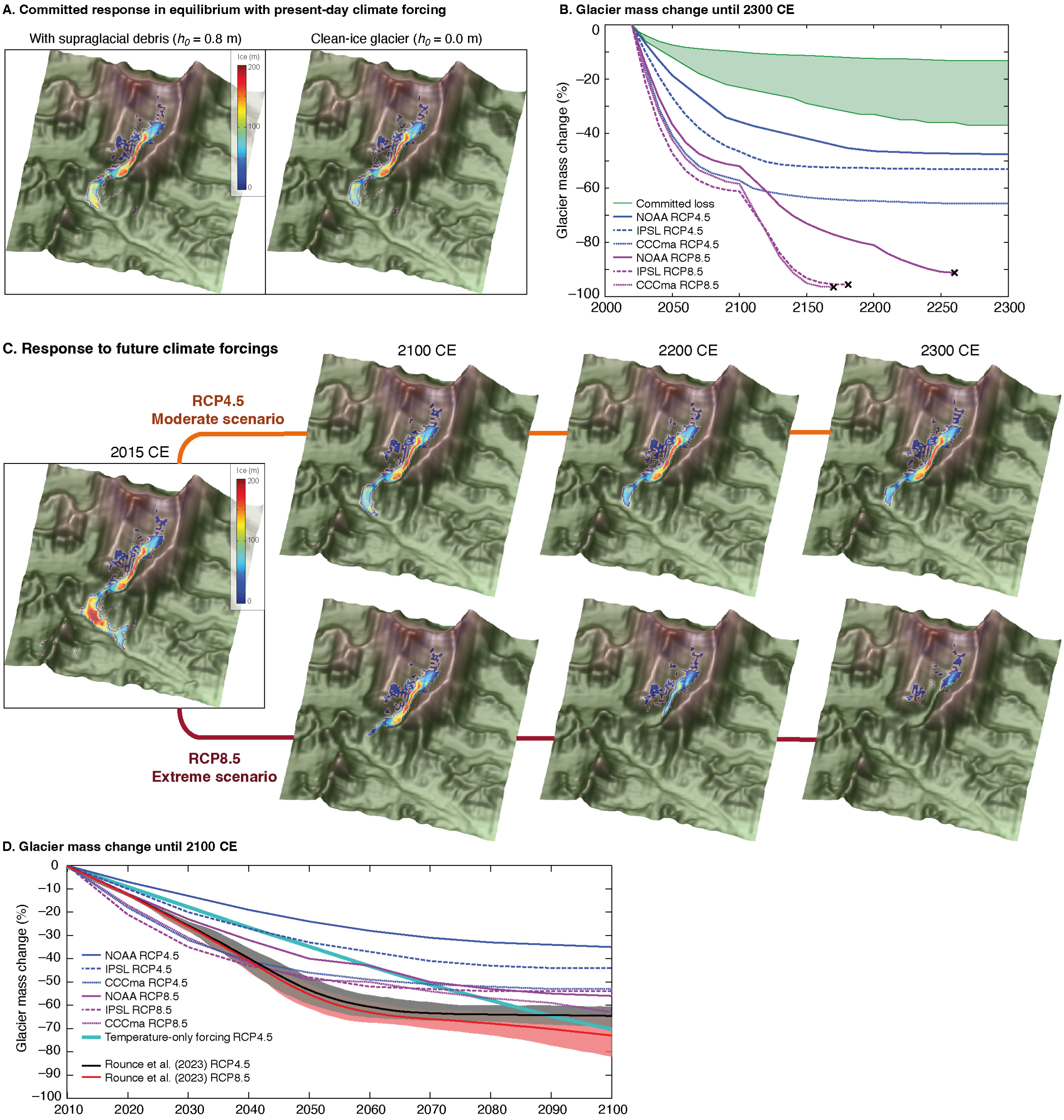

Figure 7. Future glacier volume change projections. (a) Equilibrium ice thickness accounting for the committed response to recent climate change using the downscaled NOAA RCM climate forcing with and without the effect of sub-debris melt. (b) Simulated glacier volume change from the present day (2015–2020 CE) until 2300 CE under RCP4.5 and RCP8.5 for the three downscaled RCMs. The black crosses mark when ice flow has declined sufficiently that the glacier is considered almost absent or no longer viable. The green shading shows the range of the committed volume loss due to historical warming. (c) Simulated ice thickness under RCP4.5 and RCP8.5 for 2100 CE, 2200 CE and 2300 CE using the downscaled NOAA RCM climate forcing. (d) Comparison of projected shrinkage of Khumbu Glacier by 2100 CE from this study with those from Rounce et al. (2023) showing results from each of the six experiments in this study with results from RCP4.5 and RCP8.5 from Rounce et al. (2023), the equivalent result for a simulation where precipitation does not change from the present-day value.

Appendix A

1. Downscaled climate model results

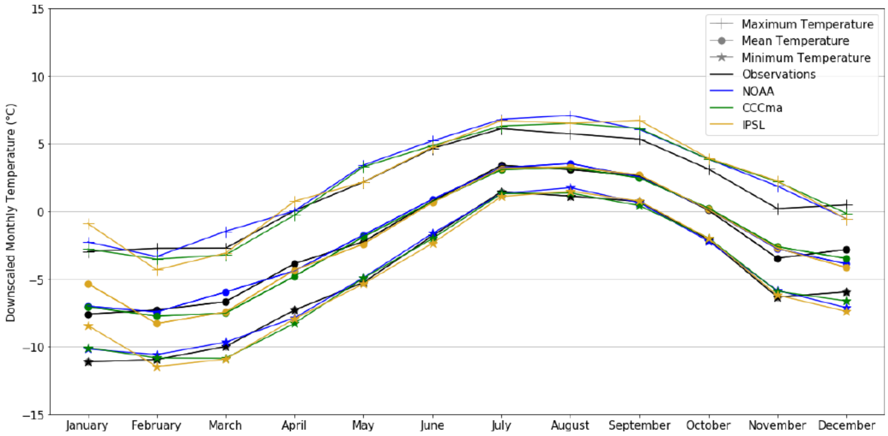

Figure A1: Downscaled monthly mean, maximum, and minimum temperature calculated for the present day time slice.

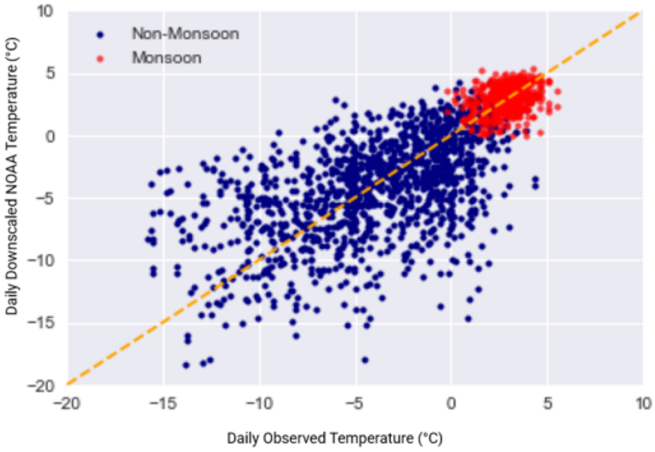

Figure A2: Daily downscaled temperature from the NOAA RCM against observations, split by monsoon/non-monsoon with a 1:1 line to aid analysis of the temperature distributions (dashed orange line).

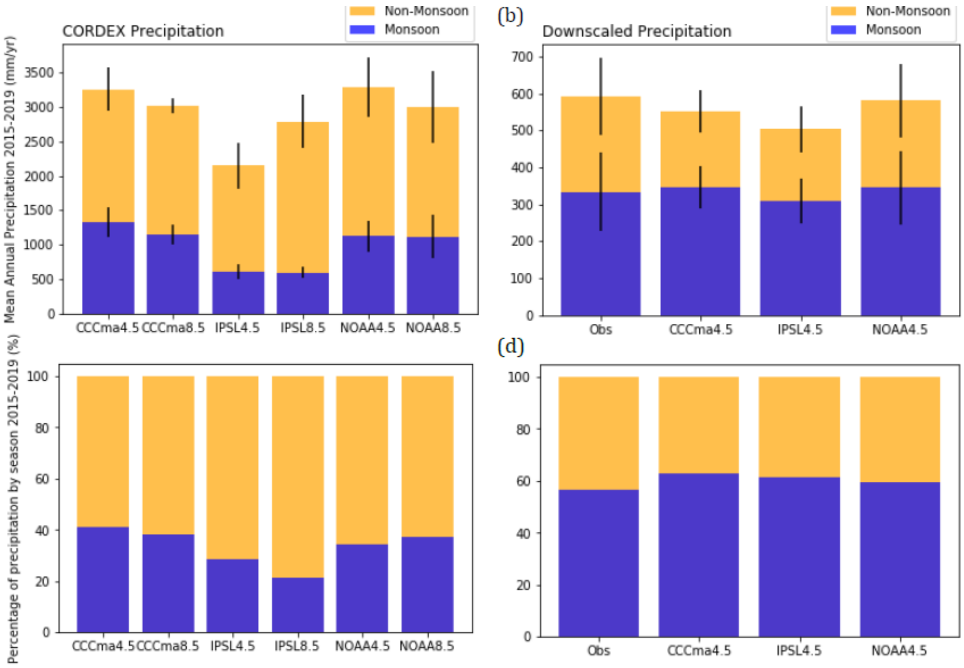

Figure A3. Annual precipitation totals for non-monsoon and monsoon months before and after downscaling with standard deviation between selected years shown by black bars (a and b) and as their seasonal percentages (c and d). The annual precipitation matches measurements in the southern Dudh Koshi catchment for the gridbox nearest to Khumbu Glacier is located at 27.9065056°N, 86.4352951°E which is 2,100 m a.s.l..

2. Regional Climate Model analysis and selection

Three of the six available CORDEX South Asia RCMs (NOAA, CCCma, IPSL) were selected as discrete scenarios that span the range of possible future precipitation conditions (Table 1); either wet, moderate, or dry climate in 2080–2100 CE (Figure A4). The raw RCMs significantly overestimate annual total precipitation by at least a factor of five for the selected gridpoint which is corrected for by downscaling these results using AWS data.

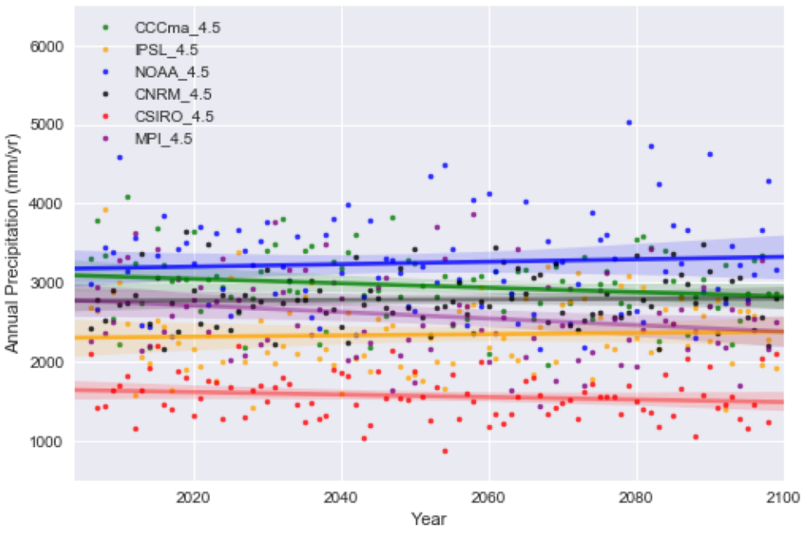

Figure A4: Annual precipitation sums (dots) with fitted trend line from the start of the RCP experiments (2006) until the end (2100) for each of the six Indian Institute for Tropical Meteorology CORDEX models for RCP4.5.

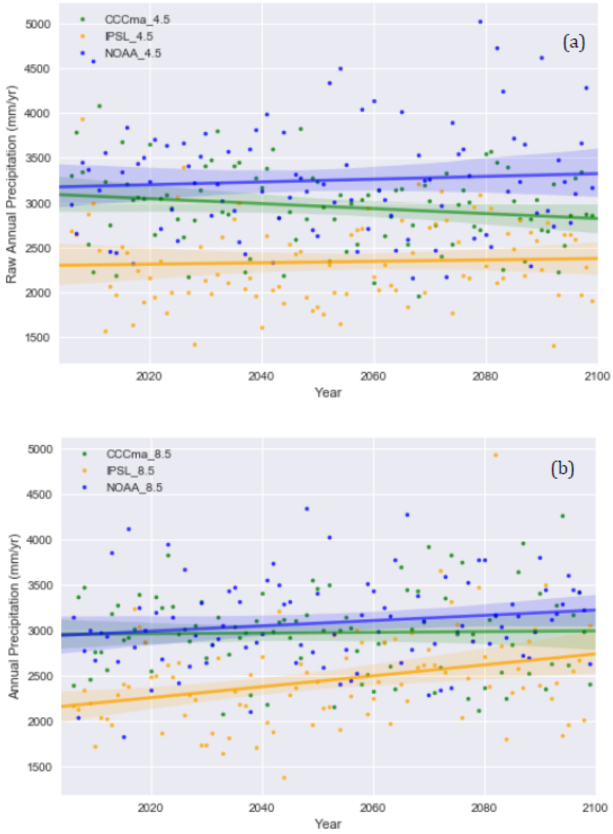

Figure A5: Annual precipitation sums (dots) with fitted trend line from the start of the RCP experiments (2006) until the end (2100) for the three selected of the six CORDEX models for RCP4.5 (a) and 8.5 (b).

3. Downscaling parameters and method

Though minimum and maximum temperature are not required to force COSIPY, these were downloaded and statistically downscaled using QM with normal distribution to aid disaggregation to an hourly time step using MELODIST. Quantile mapping for the CORDEX wind speed data was found to be ineffective when analysing the time series output against observations, both for the absolute wind speed as well as the reduced day-on-day variability seen during the monsoon. Therefore, GARD was used instead. This is a simple statistical analogue regression downscaling method appropriate for pointwise downscaling.

Table A1: RCM-derived parameters and the method used for downscaling or bias correction.

RCM-derived parameters	**Downscaling/bias correction method**	**Parametric distribution model (for QM)**	**References**
Precipitation (kg per m^2 per s, converted to mm day^{-1})	Quantile mapping (QM)	Gamma	Vrac et al., 2007; Piani et al., 2010
Mean temperature (K) Minimum temperature (K) Maximum temperature (K)	QM	Normal / Gaussian	Li et al., 2010, Gupta et al., 2016; Luo et al., 2018
Incoming shortwave (W m^{-2}) Incoming longwave (W m^{-2}) Relative humidity (%)	QM	Beta	Ruane et al., 2015
Pressure (hPa)	Bias correction	N/A	N/A
Wind speed (m s^{-1})	Regression downscaling	N/A	Gutmann et al., 2022

4. Meteorological distribution across the model domain

Temperature and precipitation were interpolated across the 100 m DEM using linear lapse rates:

$$V_{interp} = (V) + (Z_{pixel} - Z_{station}) \cdot LR$$

where V_{interp} is the variable to be interpolated, V is the hourly variable in question (e.g. temperature or precipitation), Z_{pixel} is the elevation (m.a.s.l.) of the target pixel in the domain, $Z_{station}$ the elevation (m) of the station, and LR is the lapse rate for that variable. Note that the distribution is from a prescribed elevation, not from the exact location of the AWS. The lapse rates were calculated from meteorological observations, as described below.

The mass balance sensitivity to temperature lapse rates that differed depending on season or time of day were examined, showing a lesser impact on glacier-wide mass balance than in other studies due to the large elevation range of Khumbu Glacier where a smaller fraction of the glacier relative to total area is located along the zero degree isotherm (*cf.* Yala Glacier; Immerzeel et al., 2014). Lapse rates that changed depending on season and time of day (given marked monsoonal and nocturnal lowering of lapse rates) averaging –0.00554 °C m^{-1} were calculated and, following integration with the glacier model, produced glacier-wide mass balance and spatial calculations that were closest to those observed, including maximum rates of surface lowering being observed in the upper ablation area where the debris layer is thinnest (Fig. 1d).

Analysis of meteorological observations made between 2,600 m and 5,600 m a.s.l. from the Ev-K2-CNR and Glacioclim networks indicated that precipitation lapse rates were weak, slightly negative or absent across the Dudh Koshi catchment, confirming the observations of Salerno et al. (2015) and Yang et al. (2017). Given the high incidence of missing precipitation data from high-elevation AWS, the undercatch of snow associated with tipping bucket rain gauges, and the absence of precipitation measurements above 5,600 m a.s.l. precipitation was not varied with elevation. To test the sensitivity of precipitation to elevation, COSIPY was forced by a gridded climate distributed using weak negative, weak positive, and no precipitation gradients. The results of these experiments were used to force the glacier model, and the simulated historical glacier evolution was similar, with only a 10 m difference in the maximum ice thickness between simulations with different precipitation lapse rates.

Direct solar radiation across the model domain was corrected by the slope, azimuth, and shadowing potential of each pixel (Wohlfahrt et al., 2016; Sauter et al., 2020). A footprint-weighted correction was also applied to horizontal measurements of net radiation. The fraction of diffuse incoming shortwave radiation was estimated by using the ratio of total shortwave (global) radiation and potential shortwave radiation to define a clearness index (Wohlfahrt et al., 2016). This clearness index was used to calculate diffuse radiation, which is calibrated with data from Neustift, an eddy covariance station in the Austrian Alps (Wohlfahrt et al., 2008). The distributed radiative fluxes were compared with high-elevation stations for 2019 to assess the efficacy of this method across the domain. Pressure was distributed across the domain by first calculating sea level pressure (*cf.* Lente and Osz, 2020) and then interpolated with the barometric equation. The relative humidity gradient was calculated as –0.002 % per m from Ev-K2-CNR and Glacioclim networks and validated with National Geographic network to capture trends at higher elevations (Matthews et al., 2020). Wind speed was assumed to be uniform across the domain.

Appendix B

1. COSIPY surface energy balance modelling

COSIPY integrates a surface energy and mass balance model with a multi-layer snow and ice model (Weidemann et al., 2018). It thereby resolves all energy fluxes *(F)* at the ice surface that contribute to surface melt *(Qmelt):*

$$F = SWin \cdot (1-\alpha) + LWin + LWout + Qsens + Qlat + Qg + Qliq$$

Where $SWin$ is incoming shortwave radiation, α is albedo, $LWin$ and $LWout$ are incoming and out-going longwave radiation and *Qsen*s, *Qlat*, *Qg* and *Qliq* are the sensible, latent and ground heat fluxes (Oerlemans et al., 2001), and the heat flux from liquid precipitation. The latter is often neglected in melt models (Cuffey and Paterson, 2010), but is of particular importance here as the Indian Summer Monsoon brings a significant amount of liquid precipitation to the lower reaches of Khumbu Glacier. If *Qlat* is negative, ablation will occur through sublimation even in instances where surface temperature (T_s) and/or air temperature (T_{air}) are well below the melting point (0°C). The resulting *F* is equal to the energy available for surface melt (*Qmelt*) when T_s is at melting point (0°C). T_s is used to calculate *LWout, Qsens*, *Qlat*, *QG* and partition solid and liquid precipitation. When T_s exceeds the melting point it is reset to 0°C (273.15 K) and the residual *F* fluxes equal *Qmelt*. In this instance, subsurface melt is triggered when the energy fluxes, for example, penetrating $SWin$ warm the ice layer so that T_s exceeds the melting point of ice (Sauter et al., 2020).

The exchange processes at the surface, including energy release and consumption with phase changes, control temperature distribution and phase changes within the glacier (comprised of horizontal ice and snow layers). The coupling of the surface energy balance component with a multi-layer subsurface snow and ice model accounts for meltwater refreeze and percolation, with the meltwater produced from the surface melt calculations, acting as an input. The mass balance is calculated at an hourly resolution, with the accumulation rates coming from this refreeze of meltwater, and the accumulation of solid precipitation on the ice surface, as well as deposition of water vapour (Sauter et al., 2020). Ablation is by subsurface and surface melt and sublimation. The turbulent fluxes and energy balance components across Khumbu Glacier were explored across a three-year period to assess the performance of COSIPY and understand their relative spatial importance.

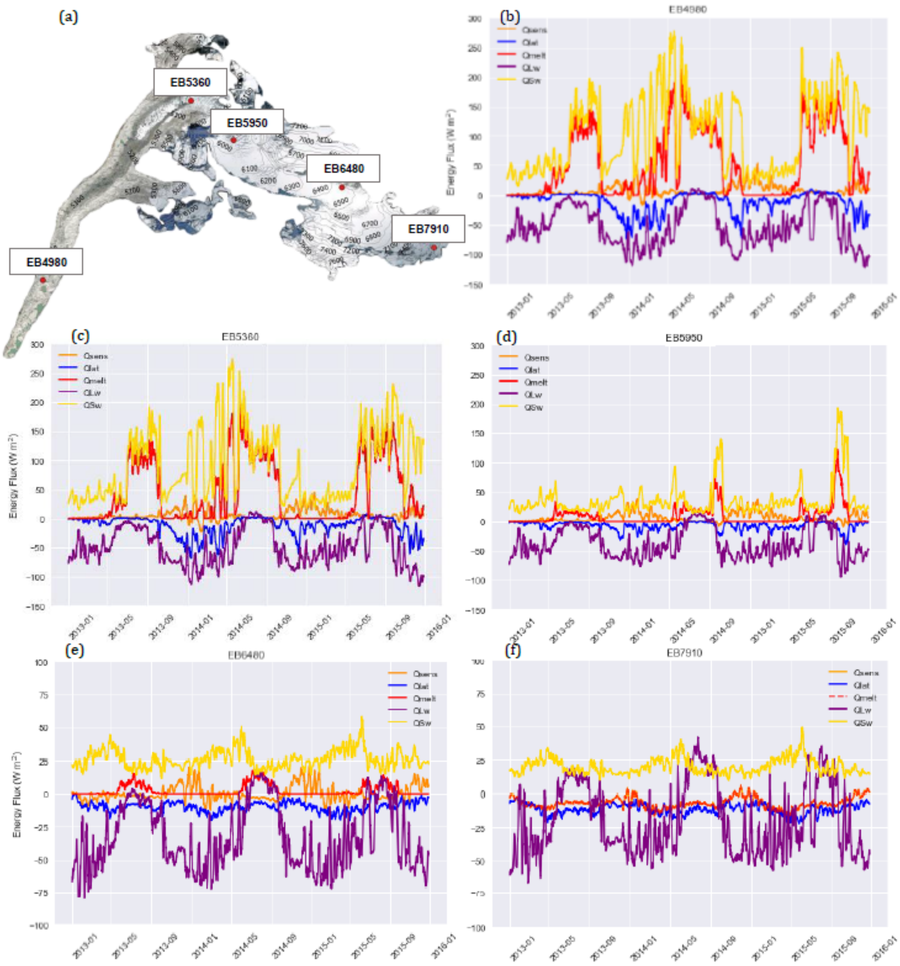

Figure B1: (a) Locations of energy balance (EB) points used for energy flux and melt components analysis (named after corresponding altitude e.g., EB6480) and (b-f) 5-day average of energy fluxes across study period for each site. Note that scales are different for (e) and (f) compared to (b)-(d) due to the marked difference in absolute values.

Calculated *SWin* matched well with observations from Ev-K2-CNR, GlacioClim and high elevation networks (Matthews et al., 2020), indicating the radiation model performs fairly well despite the extreme terrain. Net shortwave radiation contributes the largest energy input to the glacier surface at lower elevations, correlating most strongly with the energy available for melt, or *Qmelt* with a mean correlation coefficient of 0.79. There was high temporal variability related to varied cloud cover exhibited in the hourly *SWin* forcing and fluctuating albedo during the warmer months with the melting of the snowpack. The high SWin the upper reaches indicate the low net shortwave radiation is not through topographic shading. Net shortwave radiation is correlated with albedo (r = 0.86), and the persistence of snow throughout much of the year will reduce *Qmelt*. Net longwave radiation (*QLW*) also contributes to *Qmelt* as the pattern of both fluxes correspond. Between 5,900–7,900 m a.s.l., *QLW* sometimes rises above zero during the monsoon, most likely from heavy cloud cover and increased temperatures relative to the glacier surface. *Qlat* is almost zero at the lower elevation sites as the arrival of the monsoon brings higher *RH*, and this pattern is similar but dampened at the higher elevations. At EB7910, *Qmelt* correlates exactly (r = 1) with the sensible heat flux.

The energy available for ablation peaks in the pre-monsoon and monsoon, bringing higher rates of sublimation and subsurface melt. Modelled sublimation occurs at all elevations, with the highest cumulative loss at EB7910 near to South Col where sublimation dominates (not shown). Sublimation rates are increasingly tied to seasonality down-glacier, with rates at site EB4980 located on the lower section of the tongue increasing from April until the start of the monsoon in July. At EB7910 sublimation only slightly slowed from December until May. Subsurface melt at or above the ELA (5,950 m.a.s.l) is negligible. At the lower elevations sub-surface melt dominates, with a stronger seasonal cycle related to surface temperatures. The interannual variability in subsurface melt is tied to surface temperatures, though low simulated subsurface melt rates in the first year are likely largely due to the initial snow cover persisting, shielding the sub-surface from surface temperatures until the subsurface adapts to local conditions. Refreeze occurred at all sites and the onset was staggered with increased elevation, though for all sites absolute values were low. The higher *Qlat* with the monsoon brings higher deposition to the glacier at the lower elevations, with negligible rates at higher elevations. Similar absolute values and patterns are seen for condensation.

The glacier ice surface roughness (z_0) is defined as 1.7 mm (Table B1), which is a reasonable estimate for clean-ice glaciers (Mölg et al., 2012). The z_0 values reported within the literature vary widely even for clean-ice glaciers, and so two substantially different z_0 values are used. Values of 0.1 mm were measured at Midtre Lovénbreen, Svalbard (Irvine-Fynn et al., 2014) and August-One Glacier, China (Guo et al., 2018), and of 6.9 mm on the clean-ice section of the Haut Glacier D'Arolla (Brock et al., 2006). These values were adopted as endmembers of the likely range in z_0 values. Overall, adjusting z_0 had minimal impact on glacier mass balance, though a higher (lower) z_0 did result in slightly increased (decreased) mass balances. The albedo values of the three glacier components (Table B1) were perturbed by 5%. There was a strong response of the glacier mass balance to changing snow albedo. Reducing snow albedo by 0.05 led to a 65% reduction in mass balance of 2.21 m w.e.. Ablation (accumulation) rates were 3.7 m w.e. (1.75 m w.e.) higher relative to the reference simulation for this perturbation. This further supports the importance of *QSW* to ablation rates. Varying albedo values for firn and ice revealed a lower sensitivity of glacier mass balance relative to snow albedo.

Table B1: Glaciological constants, with α being albedo (of fresh snow, firn and ice), *t** decay time from snow to firn , *d** the constant for the effect of snow depth on albedo, and z_0 surface roughness length. The albedo values are widely used within the literature for clean. z_0 values are less well parameterised with high spatial variability across glacier surfaces. Testing revealed highest sensitivity of mass balance to $\alpha_{freshsnow}$ relative to the other parameters.

Parameter	**Value**	**Unit**	**Source**
$\alpha_{freshsnow}$	0.85	-	Mölg et al. 2012; Wagnon
α_{firn}	0.6	-	Knap and Oerlemans, 1996; Mölg et al. 2012
α_{ice}	0.3	-	Mölg et al. 2012
t*	20	days	Mölg et al. 2012
d*	1.0	cm	Mölg et al. 2012
Z_{0snow}	0.24	mm	Gromke et al., 2011
Z_{0firn}	4.0	mm	Brock et al., 2006
Z_{0ice}	1.7	mm	Brock et al., 2006
Z_0 ageing length (linearly from z_{0snow} to z_{0firn})	60	days	Mölg et al. 2012

2. Glacier modelling of Khumbu Glacier through the late Holocene to the present day

Khumbu Glacier (RGI2000-v7.0-G-15-08331) is 16.0 km long, with an area of 26.4 km^2, the median glacier elevation is 6,025 m a.s.l. from the terminus at 4,879 m a.s.l. to the headwall at 7,981 m a.s.l. (RGI 7.0 Consortium, 2023). The debris-covered tongue has an area of 6.2 km^2 (23% of the total glacier). Reconstruction of Khumbu Glacier using terrestrial cosmogenic nuclide dating of boulders on the surface of ice-marginal moraine crests shows that since the late Holocene (1.3 ± 01 ka; Hornsey et al., 2022). The Little Ice Age (LIA) maximum of Khumbu Glacier occurred about 500 years before present consistent with ages produced for similar moraines elsewhere in the central Himalaya (Hornsey et al., 2022; Rowan, 2017). Prior to the LIA maximum, Khumbu Glacier had a slightly greater extent during the late Holocene and is likely to have reached the LIA extent by the formation of large moraines that enclosed the LIA glacier and drove the ice mass to thicken rather than expand in area. During the LIA advance, Khumbu Glacier transitioned from a clean-ice glacier with high velocities and efficient export of debris to moraines to an debris-covered glacier with lower velocities initiated by a reduction in ice flux promoted by thickening supraglacial debris (Rowan et al., 2015). As a starting point for our transient simulations of Khumbu Glacier, we reconstructed the late Holocene glacier from an ice-free domain using an ELA of 5,325 m a.s.l. and a mean annual atmospheric lapse rate of –0.004°C per m over a 5000-year spin-up simulation and through the LIA as an increase in ELA of 50 m to 5,375 m a.s.l. over 500 years following Rowan et al. (2015, 2021). We tested a range of atmospheric lapse rates from 0.003°C per m^{-1} to 0.006°C per m^{-1} maintaining the same ELA, which resulted in a difference in ice volume of 0.4×10^9 m^3 and no change in glacier length.

We examined the uncertainty in accumulation resulting from the application of a calculation to move snowfall from slopes susceptible to avalanching. Observations of high-elevation Himalayan glaciers, including Khumbu Glacier, indicate that up to 75% of accumulation occurs by avalanching rather than direct snowfall (Benn and Lehmkuhl, 2000). Avalanching affects Khumbu Glacier in two ways; firstly by moving snow from steep hillslopes onto the glacier surface, thus increasing accumulation from that calculated from direct snowfall onto the glacier surface, and second by redistributing snow across steep sections of the glacier surface. Therefore, if avalanching was not consider in the climate-glacier model, then the accumulation of snow calculated using COSIPY that occurred within the Khumbu Glacier catchment but outside of the RGI glacier outline would have no impact on glacier mass balance, resulting in an underestimation of ice volume. Redistribution on snow across the glacier surface is also an important process affecting the mass balance of Khumbu Glacier, and in a simulation where accumulation occurred at a uniform rate of 2.0 w.e. m a^{-1} across the accumulation area in the Western Cwm, when avalanching and downslope distribution of snow onto the glacier surface were not simulated the resulting glacier had a similar extent but a total volume more than double that of the glacier simulated with avalanche redistribution of snow, because mass was not redistributed effectively across steep sections of the glacier surface.

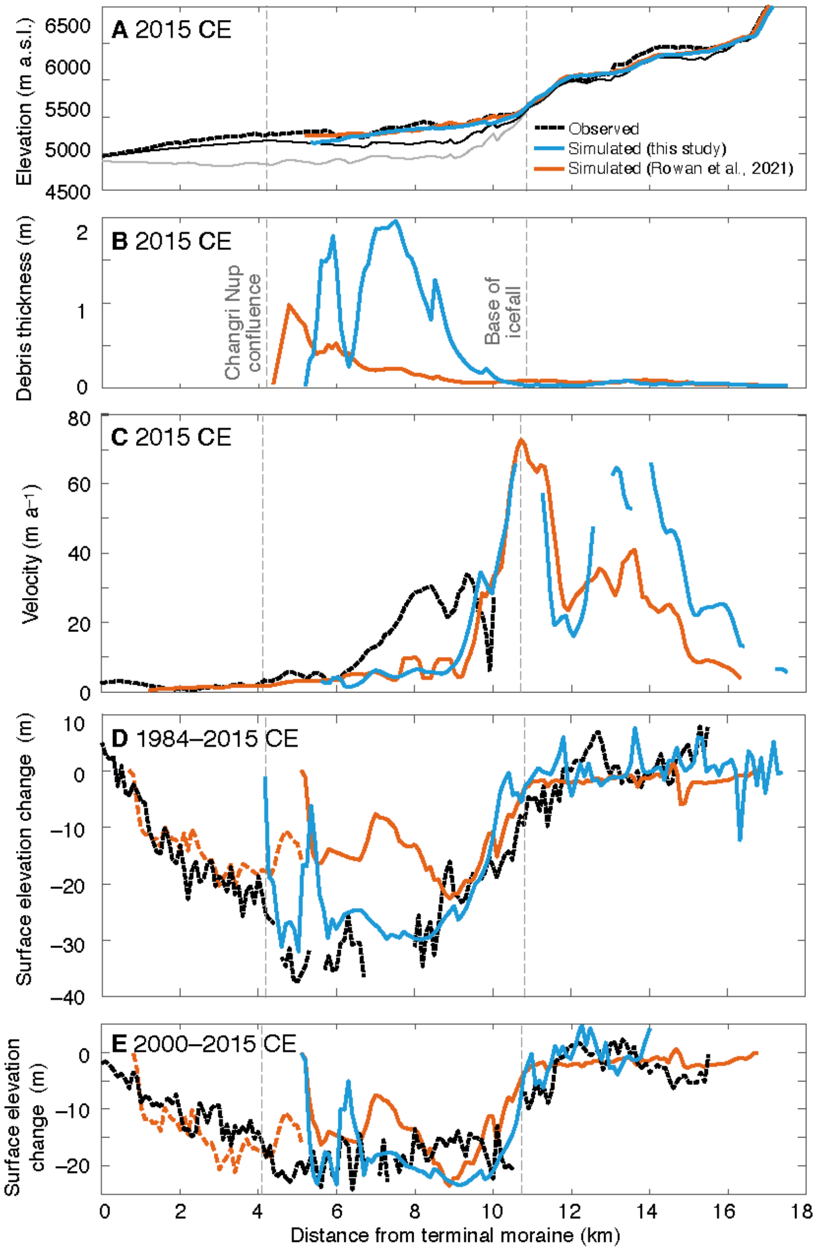

Figure B2. Evaluation of present-day simulation showing; (a) mean simulated ice thickness calculated from a 500 m-wide swath profile along the central flowline of the glacier. Subglacial topography including the dynamically detached debris-covered tongue is shown by the solid black line and subglacial topography used in the entire glacier simulations in Rowan et al. (2015) is shown for comparison by the lowermost grey solid line. The estimated present-day ice thickness (Farinotti et al., 2019) is shown by the dashed black line. (b) mean simulated debris thickness, (c) simulated and observed velocities from the NASA MEaSUREs ITS_LIVE project (Dehecq et al., 2019), and simulated and observed mean surface elevation change between (d) 1984–2015 CE and (e) 2000–2015 CE compared with results from the simulations in this study and those in Rowan et al. (2021) where further information about the model evaluation can be found.

Additional references for Appendices

Brock, B.W., Willis, I.C. and Sharp, M.J., 2006. Measurement and parameterization of aerodynamic roughness length variations at Haut Glacier d'Arolla, Switzerland. Journal of Glaciology, 52(177), pp.281-297. https://doi.org/10.3189/172756506781828746

Gromke, C., Manes, C., Walter, B., Lehning, M. and Guala, M., 2011. Aerodynamic roughness length of fresh snow. Boundary-Layer Meteorology, 141, pp.21-34. https://doi.org/10.1007/s10546-011-9623-3

Guo, S., Chen, R., Liu, G., Han, C., Song, Y., Liu, J., Yang, Y., Liu, Z., Wang, X., Liu, X. and Wang, L., 2018. Simple parameterization of aerodynamic roughness lengths and the turbulent heat fluxes at the top of midlatitude August-One Glacier, Qilian Mountains, China. Journal of Geophysical Research: Atmospheres, 123(21), pp.12-066. https://doi.org/10.1029/2018JD028875

Gupta, A. and Tarboton, D.G. 2016. A tool for downscaling weather data from large-grid reanalysis products to finer spatial scales for distributed hydrological applications. Environmental Modelling & Software. 84, pp. 50–69. https://doi.org/10.1016/j.envsoft.2016.06.014

Gutmann, E. D., J. J. Hamman, M. P. Clark, T. Eidhammer, A. W. Wood, and J. R. Arnold, 2022: En-GARD: A Statistical Downscaling Framework to Produce and Test Large Ensembles of Climate Projections. J. Hydrometeor., 23, 13545–1561, https://doi.org/10.1175/JHM-D-21-0142.1.

Irvine-Fynn, T.D., Sanz-Ablanedo, E., Rutter, N., Smith, M.W. and Chandler, J.H., 2014. Measuring glacier surface roughness using plot-scale, close-range digital photogrammetry. Journal of Glaciology, 60(223), pp.957-969. doi:10.3189/2014JoG14J032

Immerzeel, W., Petersen, L., Ragettli, S. and Pellicciotti, F. 2014. The importance of observed gradients of air temperature and precipitation for modelling runoff from a glacierized watershed in the Nepalese Himalayas. Water Resources Research. 50: 2212-2226. doi: 10.1002/2013WR014506.

Lente, G. and Ősz, K., 2020. Barometric formulas: various derivations and comparisons to environmentally relevant observations. ChemTexts, 6, pp.1-14. https://doi.org/10.1007/s40828-020-0111-6

Li, H., Sheffield, J. and Wood, E.F., 2010. Bias correction of monthly precipitation and temperature fields from Intergovernmental Panel on Climate Change AR4 models using equidistant quantile matching. Journal of Geophysical Research: Atmospheres, 115(D10). https://doi.org/10.1029/2009JD012882

Luo, M., Liu, T., Meng, F., Duan, Y., Frankl, A., Bao, A. and De Maeyer, P. 2018. Comparing bias correction methods used in downscaling precipitation and temperature from regional climate models: A case study from the Kaidu River basin in western China. Water. 10(8), pp. 1046. https://doi.org/10.3390/w10081046

Mölg, T., Maussion, F., Yang, W. and Scherer, D., 2012. The footprint of Asian monsoon dynamics in the mass and energy balance of a Tibetan glacier. The Cryosphere, 6(6), pp.1445-1461. https://doi.org/10.5194/tc-6-1445-2012

Knap, W.H. and Oerlemans, J., 1996. The surface albedo of the Greenland ice sheet: satellite-derived and in situ measurements in the Søndre Strømfjord area during the 1991 melt season. Journal of Glaciology, 42(141), pp.364-374. doi:10.3189/S0022143000004214

Piani, C., Weedon, G.P., Best, M., Gomes, S.M., Viterbo, P., Hagemann, S. and Haerter, J.O., 2010. Statistical bias correction of global simulated daily precipitation and temperature for the application of hydrological models. Journal of hydrology, 395(3-4), pp.199-215. https://doi.org/10.1016/j.jhydrol.2010.10.024

Ruane, A. C., Goldberg, R., and Chryssanthacopoulos, J. 2015. Climate forcing datasets for agricultural modeling: Merged products for gap-filling and historical climate series estimation, Agricultural and Forest Meteorology, 200, pp. 233–248. https://doi.org/10.1016/j.agrformet.2014.09.016

Salerno, F., Guyennon, N., Thakuri, S., Viviano, G., Romano, E., Vuillermoz, E., Cristofanelli, P., Stocchi, P., Agrillo, G., Ma, Y., and Tartari, G. (2015). Weak precipitation, warm winters and springs impact glaciers of south slopes of Mt. Everest (central Himalaya) in the last 2 decades (1994–2013), The Cryosphere. 9: 1229-1247. doi: 10.5194/tc-9-1229-2015.

Vrac, M., Stein, M.L., Hayhoe, K. and Liang, X.Z., 2007. A general method for validating statistical downscaling methods under future climate change. Geophysical Research Letters, 34(18). https://doi.org/10.1029/2007GL030295

Wohlfahrt, G., Hammerle, A., Haslwanter, A., Bahn, M., Tappeiner, U. and Cernusca, A. 2008. Disentangling leaf area and environmental effects on the response of the Net Ecosystem Co2 Exchange to diffuse radiation, Geophysical Research Letters, 35(16). doi:10.1029/2008gl035090.

Wohlfahrt, G., Hammerle, A., Niedrist, G., Scholz, K., Tomelleri, E. and Zhao, P. 2016. On the energy balance closure and net radiation in complex terrain, *Agricultural and Forest Meteorology*, 226–227, pp. 37–49. doi:10.1016/j.agrformet.2016.05.012.

Yang, K., N. Guyennon, L. Ouyang, L. Tian, G. Tartari, and F. Salerno (2017). Impact of summer monsoon on the elevation-dependence of meteorological variables in the south of Central Himalaya. International Journal of Climatology. 5293: 1748-1759. doi:10.1002/joc.5293.